

THE HOT INTERSTELLAR MEDIUM OF NORMAL ELLIPTICAL GALAXIES. I. A *CHANDRA* GAS GALLERY AND COMPARISON OF X-RAY AND OPTICAL MORPHOLOGY

STEVEN DIEHL^{1,2} AND THOMAS S. STATLER¹

Draft version April 6, 2019

ABSTRACT

We present an X-ray analysis of 54 normal elliptical galaxies in the *Chandra* archive and isolate their hot gas component from the contaminating point source emission, allowing us to conduct, for the first time, a morphological analysis on the gas alone. A comparison with optical images and photometry shows that the hot gas morphology has surprisingly little in common with the shape of the stellar distribution. We observe no correlation between optical and X-ray ellipticities in the inner regions where stellar mass dominates over dark matter. A shallow correlation would be expected if the gas had settled into hydrostatic equilibrium with the gravitational potential. Instead, observed X-ray ellipticities exceed optical ellipticities in many cases. We exclude rotation as the dominant factor to produce the gas ellipticities. The gas appears disturbed, and hydrostatic equilibrium is the exception rather than the rule. Nearly all hydrostatic models can be ruled out at 99% confidence, based on their inability to reproduce the optical-X-ray correlation and large X-ray ellipticities. Hydrostatic models not excluded are those in which dark matter either dominates over stellar mass inside the inner half-light radius or has a prominently cigar-shaped distribution, both of which can be ruled out on other grounds. We conclude that, even for rather X-ray faint elliptical galaxies, the gas is at least so far out of equilibrium that it does not retain any information about the shape of the potential, and that X-ray derived radial mass profiles may be in error by factors of order unity.

Subject headings: galaxies: cooling flows—galaxies: elliptical and lenticular, cD—galaxies: ISM—X-rays: galaxies—X-rays: ISM

1. INTRODUCTION

The launch of *Chandra* and *XMM-Newton* opened a new era in our understanding of the hydrodynamic histories of galaxies and clusters. Early spectral evidence from *ROSAT* and *ASCA* (e.g. Fabbiano et al. 1994; Buote & Canizares 1997) already suggested soft diffuse gas and harder stellar point sources as the two dominant components of the X-ray emission of normal elliptical galaxies. But *Chandra* made it possible for the first time to spatially resolve a significant fraction of the point source component into individual sources, which are now believed to consist mainly of low-mass X-ray binaries (LMXBs, e.g. Sarazin et al. 2003, and references therein). This has significantly contributed to the understanding of the correlation between X-ray and blue luminosity. The L_X – L_B diagram shows a steep $L_X \propto L_B^2$ relation at the gas-dominated group and cluster scale, and gets shallower toward low X-ray luminosities for normal elliptical galaxies due to the increasing importance of the point source component (O’Sullivan et al. 2001). For these galaxies, the LMXB emission severely contaminates the diffuse hot gas emission and complicates efforts to reveal its spatial structure.

It has long been assumed that the hot interstellar medium (ISM) in elliptical galaxies is in hydrostatic equilibrium with the underlying gravitational potential (e.g.

Forman et al. 1985). The desire to make this assumption is natural since it then gives us a powerful tool to probe the host galaxy’s mass distribution. As such, radial mass profiles derived from observed X-ray pressure profiles are among the strongest providers of evidence for the existence of massive dark matter halos surrounding normal elliptical galaxies (e.g. Forman et al. 1985; Killeen & Bicknell 1988; Paolillo et al. 2003; Humphrey et al. 2006; Fukazawa et al. 2006) and have been found to be consistent with those derived from gas kinematics in spiral galaxies (Sofue & Rubin 2001, and references therein) and stellar kinematics in ellipticals (e.g. Statler et al. 1999), implying dark halos with mass profiles similar to those of isothermal spheres. Unfortunately, stellar kinematics can only probe the dark matter content out to a few optical radii. Farther out, one has to rely on X-ray mass profiles, gravitational lensing (Keeton 2001) or kinematical planetary nebula (PN) data (Napolitano et al. 2004). A recent study by Romanowsky et al. (2003) using PN data advocates a rather low dark matter contribution around some elliptical galaxies, at odds with standard Λ -CDM simulations (e.g. Springel et al. 2005). This discrepancy may be reconciled by appealing to radial orbits of the halo stars (Dekel et al. 2005), which underlines the difficulty of interpreting PN kinematics.

The assumption of hydrostatic equilibrium in elliptical galaxies has always been considered well founded and understood. That radial mass profiles consistent with other methods can be derived from it indicates that it is not seriously wrong. If hydrostatic equilibrium holds precisely, the isophotes of the hot gas emission should very nearly trace the projected potential isophotes, and

Electronic address: diehl@lanl.gov, statler@ohio.edu

¹ Astrophysical Institute, Department of Physics and Astronomy, 251B Clippinger Research Laboratories, Ohio University, Athens, OH 45701, USA

² Theoretical Astrophysics Group T-6, Mailstop B227, Los Alamos National Laboratory, P.O. Box 1663, Los Alamos, NM 87545, USA

may be used to trace the total mass distribution. Buote and collaborators use this approach to argue for a highly flattened triaxial dark matter halo in the elliptical galaxy NGC 720 (Buote & Canizares 1994; Buote et al. 2002). However, no test has been devised to verify that hydrostatic equilibrium holds precisely enough all the way through a galaxy to make this kind of inference valid.

Indeed, substantial evidence is accumulating to the contrary. Combining stellar kinematic information with X-ray observations of NGC 4472, both Ciotti & Pellegrini (2004) and Mathews & Brighenti (2003b) independently argue for a lack of hydrostatic equilibrium in this particular galaxy. Statler & McNamara (2002) argue that the extreme X-ray flattening of NGC 1700 provides a counterexample of an object that cannot be in hydrostatic equilibrium, and suggest that it is rotationally flattened. Rotational flattening might be expected for a variety of reasons (Mathews & Brighenti 2003a). A large fraction of the hot gas in elliptical galaxies is thought to come from stellar mass loss, and should carry the stellar angular momentum. A fraction of the hot gas may also be acquired externally during mergers, stripped off during close encounters, or fall in from a circumgalactic gas reservoir (Brighenti & Mathews 1998). In each case, the gas should contain significant angular momentum. In the standard cooling flow scenario the gas should slowly flow inward, conserving angular momentum and settling into a rotationally supported cooling disk (Brighenti & Mathews 1997, 1996; Kley & Mathews 1995). However, Hanlan & Bregman (2000) demonstrate, with *ROSAT* and *Einstein* data for 6 elliptical galaxies, a lack of gas disk signatures. They find ellipticities that generally do not exceed values of ~ 0.2 , whereas disk models predict ellipticities larger than ~ 0.5 .

Detailed *Chandra* and *XMM* studies of over two dozen individual early-type galaxies are now published in the literature. Many of these observations reveal systems that are morphologically disturbed, with a large variety of suggested causes. For example, Jones et al. (2002) argue for the presence of shocks in NGC 4636; Finoguenov & Jones (2001) find evidence for interactions with the central radio source in NGC 4374; and Machacek et al. (2004) suggest that NGC 1404 is moving relative to the Fornax intracluster gas. Only a few objects appear round and quiescent, such as NGC 4555 (O’Sullivan & Ponman 2004) or NGC 6482 (Khosroshahi et al. 2004). Nonetheless, the use of hydrostatic equilibrium as a fundamental assumption about the majority of early-type galaxies persists (e.g. Fukazawa et al. 2006).

The main obstacle to understanding the true physical state of the hot ISM in elliptical galaxies is the separation of the gas and unresolved LMXB contributions to the diffuse emission, which is particularly important for X-ray faint galaxies. So far, two main approaches have been employed. (1) Resolved point sources are removed, and the residual diffuse image is adaptively smoothed. It is then argued or hoped that the contribution of unresolved point sources can be neglected while interpreting the diffuse emission and that what is shown is close to the gas morphology (e.g. Buote et al. 2002). (2) The observation is separated into broad radial bins with sufficient

signal to extract and fit a spectrum with a two component model, thus spectrally separating gas and LMXBs in the radial profile (e.g. Humphrey et al. 2006). Method (1) has the obvious disadvantage that one does not know what one is looking at. One gains no information on gas morphology in X-ray faint systems which are known to be LMXB dominated. Method (2) allows some insight into the radial distribution and extent of the gas but reveals nothing about the true elliptical shape or asymmetric features.

This is the first paper in a series that analyzes data on 54 elliptical galaxies in the *Chandra* public archive. We homogeneously reanalyze the observations and introduce a new technique to isolate the gas from LMXBs. An adaptive binning technique (Diehl & Statler 2006; Cappellari & Copin 2003) is then used to reveal the morphology of the gas *alone*. We present a gas gallery and a quantitative morphological analysis. For the first time, we are able to test whether hydrostatic equilibrium generally holds in normal ellipticals, by comparing gas and stellar isophotal ellipticities in the region where the stellar mass is expected to dominate the potential. We show that the archive sample fails the test. We also examine the evidence for rotational support of the gas, and find it to be extremely weak. The subsequent papers in this series will take up the origin of the observed gas morphology (Diehl & Statler 2007a, hereafter Paper II) and address the importance of central active galactic nuclei (AGN) in reheating the gas (Diehl & Statler 2007b, hereafter Paper III).

The remainder of this paper is organized as follows. In §2 we describe the details of the data reduction pipeline, the new isolation technique and the method used to derive ellipticity profiles. In §3 we present our comparison between optical and X-ray properties and address the evidence for hydrostatic equilibrium and rotational support. We discuss the implications of our findings in §4, before we summarize in §5.

2. DATA

2.1. Sample Selection and Pipeline Reduction

We select all galaxies having non-grating ACIS-S observations with approved exposure times longer than 10 ks in the *Chandra* public archive of cycle 1-4 which are classified as E or E/S0 in the Lyon–Meudon Extragalactic Database (LEDA; Paturel et al. 1997). We remove brightest cluster galaxies and objects with purely AGN-dominated emission. This sample is almost identical to that used in a previous paper (Diehl & Statler 2005), except for the removal of two galaxies. We exclude the NGC 4782/NGC 4783 galaxy pair due to its ongoing merger and the dwarf elliptical NGC 1705 whose luminosity is two orders of magnitude smaller than that of the next largest object. Our final sample consists of 54 early-type galaxies, 34 of which are listed as members of a group in the Lyon Group of Galaxies (LGG, Garcia 1993) catalog, with 19 identified as the brightest group member. Eight are also identified as members of X-ray-bright groups in the GEMS survey (Osmond & Ponman 2004), together with 5 additional galaxies that are not listed in the LGG catalog.

We apply a homogeneous data reduction pipeline to all observations starting from their level 1 event files us-

ing CIAO version 3.1 with calibration data base 2.28. The basic data reduction steps follow the recommendations according to *Chandra*'s ACIS data analysis guide³. The newest gain file is applied and adjusted for time-dependent gain variations to account for the drift of the effective detector gains with time caused by changes in the charge transfer inefficiency. Observation-specific bad columns and pixels are removed and each observation is restricted to its good time intervals. We additionally filter each light curve by iteratively applying a 2.5σ threshold to remove background flares. The remaining light curve is then clipped at 20% above the average count rate, to match the standard of the Markevitch blank sky background files⁴. Each light curve is inspected and verified to be clean. If the entire observation is affected by a very long flare that manifests itself as an underlying "ramp" in the light curve, we flag the object and use a local background spectrum in our spectral analysis instead of blank sky fields. The background correction for the subsequent spatial analysis is not taken from the blank sky background files, but rather derived from surface brightness profile fits (see also §2.2) which will automatically correct for flux offsets from residual flares. The remaining event list is filtered to retain standard ASCA grades 0, 2, 3, 4, and 6 to optimize the signal-to-background ratio. Cosmic ray afterglows, as flagged by the CIAO tool *acis_detect_afterglow*, are removed for the purpose of source detection to minimize the number of spurious detections⁵. These photons are retained for the rest of the analysis. In practice, we find that keeping or removing the afterglows makes no difference to the results.

Our analysis is restricted to photon energies between 0.3–5 keV, maximizing the relative contribution of soft hot gas emission, while avoiding the rise of the particle background at higher energies. All quoted X-ray luminosities are restricted to this band. We split this energy range further into a soft (0.3–1.2 keV) and a hard (1.2–5.0 keV) band. To create flux-calibrated images that take the spatially dependent spectral changes into account, we create mono-energetic exposure maps in steps of 7 in PI (~ 100 eV). The observation is split into 14.6 eV-wide (the width of one PI channel) individual images. A photon-flux-calibrated "slice" is created by dividing this counts image by the energetically closest exposure map. The sum of all individual slices represents the final photon flux image. These flux-calibrated images allow an accurate flux determination even in cases where a spectral analysis is impossible due to the lack of sufficient signal.

2.2. Isolating the X-ray Gas Emission

To isolate the hot gas emission we follow the procedure outlined by Diehl & Statler (2005). A summary is repeated here with some additional details, which are essential for the morphological analysis in this paper.

We use the CIAO tool *wavdetect* to identify point sources, remove regions enclosing 95% of the source flux and refill the holes with simulated Poisson counts to obtain an image of diffuse emission. We determine uniform

background values for the soft and hard bands by extracting radial surface brightness profiles for the diffuse emission from the calibrated photon-flux images and fitting them with β , double- β and Sérsic models plus an additive constant background. The sole purpose of these fits is to determine the background value; all other fitting parameters are discarded for the subsequent analysis. As the models generally yield slightly different background values, we add half of this difference to the statistical background error. If there is insufficient signal to produce an accurate fit, we compute the average surface brightness level outside a 2.5 arcmin radius and use it as the background value. We then subtract the spatially uniform backgrounds from the photon-flux calibrated images to obtain the background corrected images of diffuse emission for the soft and hard bands. Background errors are propagated into the final gas variance image and taken into account in the subsequent analysis.

The hot gas emission is still contaminated by unresolved point sources and the incompletely removed PSF wings of resolved point sources. These contaminants must be modeled and removed to isolate the hot gas emission alone. To do this, we split the background corrected, photon-flux calibrated images into the soft band S and hard band H . Gas and point source components contribute at different levels to each band, determined by their respective softness ratios γ and δ . By expressing both bands as linear combinations of the hot gas component G and the unresolved point source component P , we can solve this system of equations to isolate the gas emission itself:

$$S = \gamma P + \delta G, \quad (1)$$

$$H = (1 - \gamma)P + (1 - \delta)G; \quad (2)$$

$$\text{thus, } G = \frac{1 - \gamma}{\delta - \gamma} \left[S - \left(\frac{\gamma}{1 - \gamma} \right) H \right]. \quad (3)$$

This decomposition depends on the softness ratios γ and δ . To determine the softness of the unresolved point sources, we first analyze the hardness ratios of resolved point sources. We find no evidence for any spatial dependence or luminosity dependence of their spectral properties. This is in agreement with studies by Irwin et al. (2003), which suggest a universal nature of LMXBs, and allows us to use the known spectral properties of resolved LMXBs as a template for their unresolved counterparts. For each galaxy, we select resolved point sources between $5''$ and 5 optical effective radii from the center to avoid the influence of the central AGN, and to minimize contributions from serendipitous background sources. We exclude high luminosity sources (> 200 counts) to ensure that the spectral fits are driven by low-luminosity sources. If more than 10 sources fulfill these selection criteria, we fit an absorbed power law model to the combined LMXB spectrum. We find that a narrow range of photon indices (1.1 to 1.8) is adequate for the point source component in all of our galaxies). To get an equivalent point source spectral model for galaxies without sufficient resolved point sources, we simultaneously fit a power-law to all low-luminosity ($L_X \leq 5 \times 10^{37}$ erg s⁻¹) LMXBs available in our complete galaxy sample. This combined fit yields a photon index of 1.603, which we adopt as the representative spectral model for source-poor galaxies. By integrating the adopted unabsorbed

³ http://cxc.harvard.edu/ciao/guides/acis_data.html

⁴ http://cxc.harvard.edu/cal/ACIS/Cal_prods/bkgcmd/acisbg/COOKBOOK

⁵ <http://cxc.harvard.edu/ciao/threads/acisdetectafterglow/>

spectral model over the soft and hard band, we derive the point source softness ratio γ .

To find the softness ratio of the hot gas component, δ , we extract a spectrum from the diffuse emission within only the inner 3 optical effective radii of each galaxy, to avoid contamination by intragroup or intracluster gas. We use an absorbed single temperature APEC thermal plasma model for the hot gas and add the adopted power-law model to represent unresolved point sources. We fix the redshift parameter to the LEDA value, while temperature, metallicity and normalizations are generally allowed to vary freely. For low signal-to-noise spectra, we fix the metallicity to the solar value. All described spectral fits are computed with the CIAO tool *Sherpa* and corrected for Galactic absorption, with the hydrogen column density fixed at the Galactic value for the line of sight, as determined by the CIAO tool *Colden*⁶. This decomposition technique removes both the unresolved point sources and the PSF wings of resolved sources, due to their universal spectral nature.

To reliably interpret the sparse gas images and to reveal any spatial features, we bin the gas images with an adaptive binning method using weighted Voronoi tessellations (Diehl & Statler 2006; Cappellari & Copin 2003)⁷ to achieve an approximately constant signal-to-noise ratio per bin of 4. In background dominated, very-low signal-to-noise regions, the required bin size can get very large and the bins occasionally “eat” into the inner emission to accrete sufficient signal. To avoid this effect, we restrict the maximum bin size for these objects, resulting in a drop of signal-to-noise per bin in the outer regions.

A few things should be kept in mind regarding our new isolation technique for the hot gas. First, we assume isothermal gas throughout the galaxy, resulting in a spatially constant δ parameter. We test the validity of this assumption by creating two-dimensional temperature maps for systems with the highest signal-to-noise data and correct the gas image for a spatially dependent δ value. Although most galaxies exhibit temperature gradients, the corrections to the gas surface brightness are generally $< 10\%$ and do not affect the overall gas morphology. For those objects that do have sufficient signal to produce a spatially dependent temperature map, the effects on ellipticity and asymmetry are negligible. Spatial temperature gradients and inhomogeneities will be examined in more detail in Paper III. However, one should be aware that strong localized temperature differences can potentially result in an over-subtraction of hotter features and under-subtraction of colder features.

Second, the region influenced by the central PSF of an AGN may be subtracted incorrectly, as the AGN softness ratio is most likely different from that of the unresolved point source component. Thus, we exclude the central regions from our analysis, and one should refrain from interpreting the gas maps at the very center. A detailed analysis of the central AGN and its effects on the overall morphology will be presented separately in Paper II. One should also keep in mind that possible direct X-ray jet signatures could be masked out in our analysis, as jet knots would most likely be identified as point sources

and thus removed.⁸

A drawback of our approach is the inevitable loss of signal. Since we are subtracting a scaled version of the hard band from the soft band to isolate the gas emission, we effectively subtract a part of the gas flux. Even though our technique corrects for this missing flux, one still loses a certain amount of signal, reducing the spatial resolution in the adaptively binned gas image. The softness of the gas comes close to that of the unresolved point sources for temperatures exceeding ~ 1.5 keV. From that point on, both components become increasingly indistinguishable and the signal-to-noise ratio of the gas image can be very low, even if there is substantial gas present. Fortunately, few objects in our sample have temperatures exceeding 1 keV.

The definite advantage of our algorithm is that we can properly isolate the hot gas emission, without assumptions about the spatial distribution of unresolved point sources, or their total flux. Even the effect of a spatially variable point source detection limit (due to variations in background levels and the changes in size and shape of the point spread function) is compensated for by our algorithm.

To give the reader a better understanding of the relative contributions of the hot gas and the resolved and unresolved point source components, we list the relative fractions in Table 1 for a radial range between $2.5''$ and $3 J$ -band effective radii (R_J). This shows that for a large subset of galaxies, a significant percentage of point sources is still unresolved and contaminates the diffuse emission, disguising the true gas morphology. In some cases (e.g. NGC 3115) the diffuse emission is even consistent with being almost entirely due to unresolved point sources.

2.3. X-ray Gas Luminosity

To calculate the total X-ray gas luminosity, we bin the calibrated gas images into adaptively sized circular annuli and produce radial surface brightness profiles, as described in Diehl & Statler (2005). X-ray surface brightness profiles of galaxy clusters and groups are generally well described by β or double- β profiles with β values between $\sim 0.5 - 1.0$. Our β model fits indicate that the gas profiles of normal ellipticals are generally shallower. For 28 out of 45 galaxies with sufficient signal to constrain the fit, the best fit β values are < 0.5 , consistent with the known relation between gas temperature and β for groups and clusters (e.g. Voit et al. 2002).

However, a β value below 0.5 yields infinite total flux when extrapolated to large radii. As this renders the β models unusable for determining total luminosities, we adopt the well-known Sérsic models instead. The Sérsic model has the advantage of yielding finite fluxes and produces equivalently good fits. The values for our best Sérsic model fits are published in an earlier paper (Diehl & Statler 2005). We derive X-ray gas luminosities by summing the calibrated gas images over the field of view, and use the model fits to correct for missing flux outside the field of view. The luminosities listed in Table 1 are also corrected for absorption effects by multi-

⁶ <http://cxc.harvard.edu/toolkit/colden.jsp>

⁷ <http://www.phy.ohio.edu/~diehl/WVT>

⁸ NGC 315 is the only object in our sample with a conspicuous jet. We have verified by eye that the jet is removed by our procedure.

TABLE 1
Chandra X-RAY PROPERTIES

Name	ObsId	τ^a	f_{Gas}^b	f_{unres}^b	f_{resol}^b	$L_{X,\text{Gas}}^c$	ϵ_X^d	PA_X^d
IC1262	2018	31	58 ± 15%	41 ± 15%	1 ± 1%	$2.0 \pm 1.7 \times 10^{43}$	0.43 ± 0.09	69 ± 11
IC1459	2196	52	58 ± 10%	12 ± 10%	31 ± 1%	$4.3 \pm 3.2 \times 10^{40}$	0.16 ± 0.08	32 ± 20
IC4296	3394	24	74 ± 10%	7 ± 9%	18 ± 1%	$1.1 \pm 0.4 \times 10^{41}$	0.28 ± 0.06	55 ± 14
NGC0193	4053	29	85 ± 13%	10 ± 9%	5 ± 1%	$2.5 \pm 0.8 \times 10^{41}$
NGC0315	4156	52	58 ± 10%	32 ± 10%	10 ± 1%	$9.4 \pm 3.4 \times 10^{40}$	0.13 ± 0.16	14 ± 32
NGC0383	2147	43	49 ± 10%	35 ± 10%	16 ± 1%	$< 7.5 \times 10^{41}$	0.23 ± 0.09	114 ± 25
NGC0404	870	24	94 ± 43%	0 ± 42%	6 ± 2%	$< 2.1 \times 10^{38}$
NGC0507	317	26	69 ± 13%	30 ± 13%	1 ± 1%	$> 5.7 \times 10^{42}$	0.13 ± 0.17	91 ± 33
NGC0533	2880	35	89 ± 19%	9 ± 18%	2 ± 1%	$9.6 \pm 3.5 \times 10^{41}$	0.37 ± 0.05	26 ± 3
NGC0720	492	34	74 ± 10%	15 ± 9%	12 ± 1%	$9.3 \pm 2.7 \times 10^{40}$	0.09 ± 0.07	75 ± 28
NGC0741	2223	29	58 ± 11%	21 ± 11%	22 ± 1%	$3.2 \pm 1.3 \times 10^{41}$	0.24 ± 0.05	162 ± 13
NGC0821	4006	13	17 ± 23%	5 ± 87%	78 ± 54%	$< 3.3 \times 10^{40}$
NGC1132	801	12	83 ± 16%	16 ± 16%	1 ± 1%	$> 9.1 \times 10^{42}$	0.08 ± 0.24	40 ± 46
NGC1265	3237	82	15 ± 8%	38 ± 8%	47 ± 5%	$< 1.1 \times 10^{42}$
NGC1316	2022	26	78 ± 13%	5 ± 13%	18 ± 1%	$5.7 \pm 2.1 \times 10^{40}$	0.33 ± 0.06	14 ± 13
NGC1399	319	24	85 ± 23%	7 ± 23%	8 ± 1%	$> 7.9 \times 10^{41}$	0.34 ± 0.04	179 ± 7
NGC1404	2942	29	94 ± 16%	1 ± 16%	5 ± 1%	$1.7 \pm 0.4 \times 10^{41}$	0.06 ± 0.07	63 ± 26
NGC1407	791	43	70 ± 10%	18 ± 10%	12 ± 1%	$1.0 \pm 0.3 \times 10^{41}$	0.13 ± 0.06	165 ± 16
NGC1549	2077	20	52 ± 10%	18 ± 9%	31 ± 2%	$> 2.0 \times 10^{40}$
NGC1553	783	19	61 ± 13%	24 ± 13%	15 ± 1%	$2.8 \pm 2.6 \times 10^{40}$	0.57 ± 0.14	90 ± 15
NGC1600	4283/4371	49	79 ± 13%	17 ± 12%	4 ± 1%	$> 1.2 \times 10^{42}$	0.24 ± 0.09	178 ± 17
NGC1700	2069	39	85 ± 14%	7 ± 14%	9 ± 1%	$> 3.2 \times 10^{41}$	0.20 ± 0.06	89 ± 12
NGC2434	2923	25	69 ± 9%	9 ± 6%	21 ± 1%	$2.6 \pm 2.0 \times 10^{40}$
NGC2865	2020	25	34 ± 21%	60 ± 19%	6 ± 2%	$< 9.9 \times 10^{40}$
NGC3115	2040	14	2 ± 9%	35 ± 8%	63 ± 5%	$< 8.7 \times 10^{39}$
NGC3377	2934	39	15 ± 22%	0 ± 15%	85 ± 10%	$< 6.1 \times 10^{39}$
NGC3379	1587	30	14 ± 4%	11 ± 4%	75 ± 2%	$< 6.3 \times 10^{39}$
NGC3585	2078	35	32 ± 7%	19 ± 5%	48 ± 3%	$> 4.2 \times 10^{39}$
NGC3923	1563	16	74 ± 9%	11 ± 8%	15 ± 1%	$4.3 \pm 1.3 \times 10^{40}$	0.15 ± 0.10	44 ± 25
NGC4125	2071	63	80 ± 13%	1 ± 13%	19 ± 1%	$7.2 \pm 2.7 \times 10^{40}$	0.24 ± 0.11	71 ± 10
NGC4261	834	31	63 ± 11%	18 ± 10%	19 ± 1%	$4.8 \pm 1.1 \times 10^{40}$	0.08 ± 0.08	108 ± 35
NGC4365	2015	40	44 ± 8%	14 ± 8%	41 ± 1%	$> 3.8 \times 10^{40}$
NGC4374	803	28	86 ± 18%	5 ± 18%	9 ± 1%	$5.9 \pm 1.3 \times 10^{40}$	0.38 ± 0.06	116 ± 7
NGC4406	318	14	89 ± 12%	10 ± 12%	2 ± 1%	$> 1.0 \times 10^{42}$	0.17 ± 0.10	113 ± 24
NGC4472	321	35	83 ± 16%	12 ± 16%	5 ± 1%	$> 8.5 \times 10^{41}$	0.12 ± 0.04	136 ± 13
NGC4494	2079	19	0 ± 2%	43 ± 10%	57 ± 5%	$< 2.1 \times 10^{40}$
NGC4526	3925	38	55 ± 12%	8 ± 10%	37 ± 2%	$8.8 \pm 7.5 \times 10^{39}$	0.07 ± 0.15	1 ± 43
NGC4552	2072	53	80 ± 10%	4 ± 10%	16 ± 1%	$2.1 \pm 1.2 \times 10^{40}$	0.21 ± 0.03	7 ± 4
NGC4555	2884	27	73 ± 20%	19 ± 18%	9 ± 2%	$> 2.3 \times 10^{41}$
NGC4564	4008	17	72 ± 23%	17 ± 15%	11 ± 2%	$> 2.0 \times 10^{39}$
NGC4621	2068	24	42 ± 11%	7 ± 9%	50 ± 4%	$1.1 \pm 0.9 \times 10^{40}$
NGC4636	323	46	95 ± 17%	3 ± 17%	3 ± 1%	$2.7 \pm 2.0 \times 10^{41}$	0.35 ± 0.04	9 ± 3
NGC4649	785	31	80 ± 11%	11 ± 11%	9 ± 1%	$1.3 \pm 0.3 \times 10^{41}$	0.08 ± 0.03	95 ± 27
NGC4697	784/4727/4728	112	57 ± 6%	6 ± 5%	38 ± 1%	$> 3.5 \times 10^{40}$	0.20 ± 0.16	80 ± 23
NGC5018	2070	25	61 ± 11%	21 ± 9%	18 ± 2%	$< 1.9 \times 10^{41}$
NGC5044	798	20	100 ± 18%	0 ± 18%	0 ± 1%	$2.6 \pm 0.8 \times 10^{42}$	0.41 ± 0.08	27 ± 10
NGC5102	2949	34	50 ± 22%	4 ± 13%	46 ± 7%	$< 1.6 \times 10^{39}$
NGC5171	3216	34	83 ± 25%	13 ± 20%	4 ± 1%	$> 2.7 \times 10^{42}$
NGC5532	3968	48	28 ± 6%	24 ± 5%	48 ± 2%	$< 8.7 \times 10^{41}$
NGC5845	4009	30	57 ± 30%	41 ± 19%	2 ± 3%	$< 5.2 \times 10^{40}$
NGC5846	788	24	95 ± 16%	4 ± 16%	2 ± 1%	$3.9 \pm 0.9 \times 10^{41}$	0.22 ± 0.05	175 ± 8
NGC6482	3218	19	90 ± 13%	9 ± 13%	1 ± 1%	$1.7 \pm 1.3 \times 10^{42}$	0.18 ± 0.09	36 ± 23
NGC7052	2931	9	90 ± 14%	6 ± 10%	4 ± 1%	$> 1.1 \times 10^{41}$	0.26 ± 0.12	54 ± 23
NGC7618	802	11	85 ± 11%	14 ± 11%	1 ± 1%	$2.3 \pm 0.9 \times 10^{42}$	0.38 ± 0.14	99 ± 16

^a Effective *Chandra* exposure time in ks after removal of flares.

^b Percentages of observed photon fluxes for the hot gas, unresolved and resolved point sources, integrated between $2.5''$ and $3R_J$.

^c Total X-ray gas luminosity in ergs s^{-1} for the 0.3 – 5 keV band.

^d X-ray gas ellipticity and position angle, evaluated between 0.6 and $0.9 R_J$.

plying a correction factor, derived from the best spectral fit, which we integrate over energy with and without absorption by the Galactic neutral hydrogen. The error bars for luminosities can get quite large for objects with very wide gas emission, where a significant fraction of flux is derived from the uncertain extrapolation to large radii. The quoted uncertainties in Table 1 also include systematic errors associated with uncertainties in the δ and γ parameters from section 2.2, as well as the uncertainty in our adopted distances (for more details, see Diehl & Statler 2005). In cases where the uncertainties are larger than the actual values due to uncertainties in the extrapolation or where we have insufficient signal for a surface brightness model fit, we determine the luminosity by summing the flux in the field of view. If the summed flux represents a detection at a $> 3\sigma$ level, we report the 3σ lower bound as a low limit in Table 1. If this is not the case, we report the 3σ upper bound as an upper limit.

2.4. X-ray Ellipticity and Position Angle Profiles

The extremely sparse nature of X-ray data generally prohibits the use of isophote fitting techniques commonly employed with optical data. Moreover, because our gas-only images are obtained from scaled differences of the hard and soft bands, they contain many individual pixels with large negative counts, which can render standard algorithms numerically unstable. To avoid this problem, we fit isophotes to the adaptively binned gas images, adapting techniques used in N -body simulations.

We populate each bin randomly with a number of pseudo counts (particles) such that the expected \sqrt{N} Poisson fluctuations match the signal-to-noise ratio in the bin. The pseudo count fluxes (masses) are chosen to give the correct flux in each bin. Isophotes are then fitted to the pseudo count distribution using an iterative algorithm that diagonalizes the second-moment tensor in a thin elliptical ring and manipulates the axis ratio until the eigenvalues match those for a constant density ring of the same shape (Statler & McNamara 2002). Twenty random realizations are run, and the distribution of complex ellipticities is used to find the mean isophotal ellipticity, major axis position angle, and errors at each radius.

Tests show that this technique is able to robustly recover simulated isophotal profiles. An example is shown in figure 1. Here we have simulated soft- and hard-band images from separate gas and point source contributions. Both gas and point sources follow different radial surface brightness models and have very different isophotal shapes. The point sources are distributed as a deVaucouleurs profile with an effective radius of 50 pixels with a constant ellipticity of 0.1 and major-axis position angle of -10° . We draw the point source luminosities from a typical power-law luminosity function with a logarithmic slope of -2.0 . We then compute the *Chandra* point spread function with the CIAO tool “mkpsf” at the source location and finally simulate Poisson counts. The gas on the other hand follows a β profile with a core radius of 20 pixels and $\beta = 2/3$. The more complicated gas ellipticity and position angle profiles are shown by the smooth curves in the middle and bottom panels of Figure 1. We assume typical softness ratios of $\gamma = 0.5$

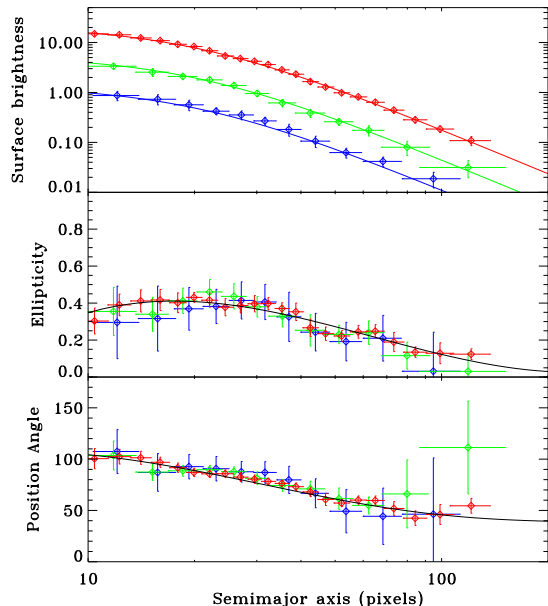


FIG. 1.— Tests of isophote fitting for simulated data with 40,000 (red), 10,000 (green), and 2,500 (blue) counts from gas. Gas emission is separated from point source emission by identifying and removing resolved sources and differencing soft- and hard-band images to remove unresolved sources (§ 2.2) and PSF wings. Isophotes are fitted to the adaptively binned gas image as described in § 2.4. Top panel shows gas surface brightness (in counts/pixel). Middle and bottom panels show isophotal ellipticity and major axis position angle. Smooth curves indicate the input profiles.

and $\delta = 0.9$ and choose the luminosities such that 60% of the counts in the simulated full-band image are from gas. This percentage is representative of the lowest end of the range for the objects in Table 1 for which isophote fitting is possible. A flat background of 0.01 counts/pixel is added to the soft and hard images before simulating discrete counts. We then go through our entire analysis pipeline: detecting point sources, removing resolved point sources, differencing the images to extract the gas map, adaptively bin, and fit isophotes as described above. Figure 1 shows the results for 40,000, 10,000, and 2,500 gas counts for a comparable radial range as is used for the real data. The isophotal profiles are recovered to within the statistical errors. Clearly, at least a few thousand counts in gas are necessary to recover accurate ellipticities. Only in cases where the entire central region is identified as consisting of several point sources and is completely blocked out, we note a systematic deviation from the input profiles. In our data this region is found to be within the central 10 pixels. Thus, we do not interpret the central $5''$ (10 pixels) in our isophotal profiles. Furthermore, accurate isophotes can be fit only where the gas surface brightness is $\gtrsim 2$ times the background. As a result, the isophotes are completely insensitive to errors in the background level.

2.5. Optical Data

Optical data for the sample galaxies are given in Table 2. We adopt the effective J -band ellipticity ϵ_J , position angle PA_J and half-light radius R_J (Table 2), as well as the absolute K magnitude from the 2MASS extended source catalog (Jarrett et al. 2000). These ellipticities and position angles are extracted at a constant magnitude level, approximately 3σ above background noise

level, generally translating to an extraction radius between 20–40 arcsec.

In addition, we extract *R*-band images from the second epoch of the Digitized Sky Survey (DSS-2R) and make use of publicly available optical surface photometry from the literature. In particular, we adopt *B* (20 galaxies), *V* (20), and *I* (19) photometry from Goudfrooij et al. (1994)⁹, *V* (21), *R* (25), and *I* (23) from Bender et al. (1988), *U* (13), *B* (15), and *R* (14) from Peletier et al. (1990) and *F814W* (9) photometry from Falcón-Barroso et al. (2006). Refer to Table 2 for details. We use the optical photometry to extract effective optical position angles PA_{opt} and ellipticities ϵ_{opt} between 0.6–0.9 R_J .

We also query the Hyperleda (Prugniel et al. 1998) data base to derive average rotational velocities between 0.6–0.9 R_J . In cases where Hyperleda does not provide the data in electronic form, we read off approximate values from published kinematic profile plots. The list of references that are used to derive the adopted rotational velocity is given in Table 2. This rotational velocity is closely related to the maximal rotational velocity but is generally a better defined quantity, as it is independent of the observational cutoff of the available kinematic data.

3. RESULTS

3.1. *X-ray vs. Optical Luminosity*

For the first time, we have spatially isolated the hot gas emission in normal elliptical galaxies to allow an unbiased morphological analysis of a large sample of objects. Figure 2 shows the X-ray gas gallery, along with the optical DSS-2 *R*-band images for each object. We rescale all images to show the same physical size of 50 kpc, except for the two closest galaxies, where we indicate the size by a separate scale bar. We have ordered Figure 2 with decreasing absolute *K* luminosity, a good indicator of the total stellar mass of the host galaxies. This is an intuitive way to visualize the large scatter in the well-known $L_X \propto L_B^2$ relation (O’Sullivan et al. 2001, and references therein), one of the elementary empirical correlations connecting X-ray and optical parameters. Its scatter shows up as a large spread in X-ray properties for galaxies that have similar stellar contents, i.e. that are close to each other in the figure. Galaxies with similar optical properties can have gas luminosities differing by orders of magnitude (e.g. NGC 5044 and NGC 1549, NGC 4555 and NGC 0533). At the same time, galaxies with comparable gas contents can have extremely different optical appearances (e.g. NGC 1404 and NGC 4649).

O’Sullivan et al. (2001) also observe a flattening of the L_X-L_B relation toward lower blue luminosities. They attribute this trend to the increasing relative importance of point source emission, which is unresolved in their ROSAT and Einstein data. Our $L_{X,\text{Gas}}-L_B$ relation, with the stellar source contribution removed (Figure 4), is consistent with a single slope, and agrees well with O’Sullivan et al. (2001)’s best fit (dashed line). Nonetheless, we still see a large scatter in this relation, covering almost two orders of magnitude in X-ray luminosity for a given absolute *B* magnitude. A recent study

by Ellis & O’Sullivan (2006) shows a similar relation between X-ray and *K*-band luminosities, with an almost identical scatter, suggesting a large scatter in X-ray luminosities as the dominant cause.

3.2. *X-ray vs. Optical Morphology*

Not only do the luminosities of the hot gas and stellar components differ vastly, there are also significant differences between the X-ray and optical morphology. Figure 2 shows that it is impossible to predict the gas morphology from looking at the stellar distribution, or vice versa. There are some optically flat galaxies with round X-ray isophotes (e.g. NGC 0720), and others with very flat X-ray emission (e.g. NGC 1700). Optically round galaxies show a similar range in X-ray ellipticities, ranging from round (e.g. NGC 1404) to flat (e.g. NGC 0533).

Many galaxies, in fact, appear asymmetrically disturbed. We discuss this asymmetry and its origin in Paper II. For now, it is important to first quantify the overall shape of the gas emission. If the gas is in true hydrostatic equilibrium, the hot gas isophotes should very nearly trace the projected equipotentials (e.g. Binney & Tremaine 1987; Buote & Canizares 1994). Thus, we construct X-ray gas ellipticity and position angle profiles, shown in Figure 5 (solid circles), with published optical profiles overlaid. The optical profiles are generally “well-behaved” and reveal only modest radial trends in their ellipticities and position angles. Optical isophotal twists, if present at all, rarely exceed a few degrees.

The X-ray profiles tell a completely different story. Often, the gas ellipticities change rapidly as a function of radius (e.g. NGC 1399, NGC 4374). These features are often accompanied by sudden changes in position angle (e.g. NGC 4636, NGC 5044). Isophotal twists in the gas emission are common, and only very few objects show profiles that are consistent with a single major axis orientation (e.g. NGC 3923, NGC 1700). In many cases isophotal twists or sudden changes in ellipticity also coincide with asymmetries in the gas images (e.g. NGC 5044).

It is generally agreed that the potentials of early-type galaxies are stellar-mass dominated inside 1 or 2 optical effective radii (e.g. Loewenstein & White 1999; Mamon & Lokas 2005; Lintott et al. 2006; Humphrey & Buote 2006). To test whether the X-ray gas flattening is consistent with hydrostatic equilibrium, we extract mean ellipticities for the hot gas emission and the starlight between 0.6 and 0.9 R_J . Figure 3 shows expanded views of the central regions of the galaxies for which gas ellipticities are measurable in this region, compared with 2MASS images. The radial range is chosen to maximize the available number of objects with valid optical and X-ray ellipticity profiles in the same interval, resulting in a subset of 24 galaxies. This subset spans more than an order of magnitude in optical luminosity and nearly two orders of magnitude in X-ray gas luminosity. Optical ellipticities are representative of the general population, and X-ray gas fractions range from 57% to 100%. Figure 6 shows that there is absolutely no correlation between optical and gas ellipticities. We have verified that this result holds for other choices of extraction annuli ranging between 0.5 and 1.2 R_J , and for different choices of optical bandpass. The large scat-

⁹ PA profiles from Goudfrooij et al. (1994) have been corrected for mirror-image flips by matching the profiles to other published photometry and DSS-2R images.

TABLE 2
 OPTICAL PROPERTIES

Name	D^a	2MASS ^b				LEDA ^c		Hyperleda ^d		Photometry ^e		
		M_K	R_J	ϵ_J	PA_J	L_B	v_{rot}	Ref.	ϵ_{opt}	PA_{opt}	Ref. ^e	
IC1262	143.8 ± 21.6	-25.43 ± 0.33	14.4	0.34	85	5.4 ± 1.7 × 10 ¹⁰	
IC1459	29.2 ± 3.8	-25.53 ± 0.28	29.1	0.19	42	4.7 ± 2.3 × 10 ¹⁰	0.27 ± 0.01	36.6 ± 0.7	T	
IC4296	51.6 ± 7.7	-26.06 ± 0.33	25.5	0.06	70	1.3 ± 0.4 × 10 ¹¹	0.13 ± 0.01	65.9 ± 1.0	U	
NGC0193	60.8 ± 9.1	-24.71 ± 0.33	14.5	0.20	55	3.0 ± 1.0 × 10 ¹⁰	
NGC0315	71.9 ± 10.8	-26.33 ± 0.33	22.9	0.22	50	1.4 ± 0.4 × 10 ¹¹	111	A	0.27 ± 0.01	42.5 ± 0.5	V	
NGC0383	73.2 ± 11.0	-25.84 ± 0.33	17.8	0.16	15	1.0 ± 0.5 × 10 ¹¹	75	A	
NGC0404	3.3 ± 0.2	7.0 ± 1.0 × 10 ⁸	
NGC0507	71.7 ± 10.8	-25.98 ± 0.33	26.1	0.12	75	1.1 ± 0.5 × 10 ¹¹	
NGC0533	77.6 ± 11.6	-26.01 ± 0.33	25.2	0.20	60	1.0 ± 0.5 × 10 ¹¹	20	B	
NGC0720	27.7 ± 2.2	-24.94 ± 0.17	27.4	0.41	145	3.6 ± 1.4 × 10 ¹⁰	0.41 ± 0.01	140.7 ± 0.1	T	
NGC0741	79.0 ± 11.8	-26.19 ± 0.33	25.9	0.38	95	1.6 ± 0.5 × 10 ¹¹	133	C	0.18 ± 0.01	87.8 ± 1.2	V	
NGC0821	24.1 ± 1.9	-24.01 ± 0.17	23.9	0.24	25	2.5 ± 0.9 × 10 ¹⁰	99	D	0.38 ± 0.01	32.3 ± 0.6	W	
NGC1132	98.2 ± 14.7	-25.70 ± 0.33	19.8	0.30	140	8.4 ± 4.2 × 10 ¹⁰	
NGC1265	109.5 ± 16.4	2.1 ± 0.9 × 10 ¹¹	
NGC1316	21.5 ± 1.7	-26.07 ± 0.17	49.8	0.30	52	9.8 ± 9.2 × 10 ¹⁰	134	E	
NGC1399	20.0 ± 1.5	-25.19 ± 0.16	36.9	0.04	150	4.9 ± 1.6 × 10 ¹⁰	31	F	0.10 ± 0.01	107.4 ± 1.0	T	
NGC1404	21.0 ± 1.8	-24.79 ± 0.19	19.3	0.12	163	3.2 ± 0.7 × 10 ¹⁰	89	F	0.14 ± 0.01	160.1 ± 1.2	T	
NGC1407	28.8 ± 3.5	-25.60 ± 0.26	36.4	0.07	20	7.6 ± 3.6 × 10 ¹⁰	< 20	G	0.04 ± 0.01	51.8 ± 0.5	T	
NGC1549	19.7 ± 1.6	-24.69 ± 0.18	29.0	0.10	143	3.4 ± 0.7 × 10 ¹⁰	60	G	0.13 ± 0.01	119.2 ± 2.5	T	
NGC1553	18.5 ± 1.5	-25.06 ± 0.17	33.9	0.34	158	4.4 ± 1.1 × 10 ¹⁰	188	H	
NGC1600	66.0 ± 9.9	-26.06 ± 0.33	24.8	0.28	5	1.3 ± 0.5 × 10 ¹¹	< 10	D	0.34 ± 0.01	7.4 ± 0.6	V	
NGC1700	54.4 ± 8.2	-25.59 ± 0.33	15.9	0.30	90	8.2 ± 3.2 × 10 ¹⁰	93	D	0.26 ± 0.01	88.1 ± 0.5	T	
NGC2434	21.6 ± 2.9	-23.78 ± 0.29	19.3	0.08	145	2.2 ± 0.6 × 10 ¹⁰	10	I	
NGC2865	37.8 ± 3.5	-24.43 ± 0.20	14.8	0.22	155	3.4 ± 1.0 × 10 ¹⁰	85	J	
NGC3115	9.7 ± 0.4	-24.05 ± 0.09	36.4	0.57	42	1.6 ± 0.9 × 10 ¹⁰	254	K	
NGC3377	11.2 ± 0.5	-22.81 ± 0.09	27.7	0.40	42	8.0 ± 1.5 × 10 ⁹	89	D	0.50 ± 0.01	41.0 ± 0.2	W	
NGC3379	10.6 ± 0.5	-23.85 ± 0.11	29.9	0.09	70	1.6 ± 0.3 × 10 ¹⁰	80	D	0.11 ± 0.01	70.6 ± 1.2	W	
NGC3585	20.0 ± 1.7	-24.81 ± 0.18	32.3	0.33	107	3.8 ± 0.9 × 10 ¹⁰	90	K	
NGC3923	22.9 ± 3.0	-25.30 ± 0.28	43.8	0.28	47	5.8 ± 1.6 × 10 ¹⁰	< 100	L	0.36 ± 0.01	47.9 ± 0.5	U	
NGC4125	23.9 ± 2.7	-25.03 ± 0.25	33.0	0.37	80	5.5 ± 1.4 × 10 ¹⁰	185	D	0.45 ± 0.01	82.0 ± 0.1	T	
NGC4261	31.6 ± 2.8	-25.24 ± 0.19	25.5	0.16	158	5.1 ± 1.2 × 10 ¹⁰	25	M	0.21 ± 0.01	158.4 ± 0.5	V	
NGC4365	20.4 ± 1.6	-24.91 ± 0.17	40.7	0.24	37	4.3 ± 1.2 × 10 ¹⁰	7	N	0.24 ± 0.01	41.6 ± 0.3	T	
NGC4374	18.4 ± 0.9	-25.10 ± 0.11	34.8	0.06	148	5.7 ± 1.0 × 10 ¹⁰	30	M	0.13 ± 0.01	125.7 ± 0.3	W	
NGC4406	17.1 ± 1.1	-25.07 ± 0.14	59.7	0.25	120	5.9 ± 1.3 × 10 ¹⁰	< 100	D	0.24 ± 0.01	123.2 ± 0.5	V	
NGC4472	16.3 ± 0.8	-25.66 ± 0.10	59.2	0.15	153	8.8 ± 1.7 × 10 ¹⁰	117	D	0.17 ± 0.01	160.6 ± 0.5	V	
NGC4494	17.1 ± 0.9	-24.16 ± 0.11	30.8	0.13	170	2.7 ± 0.4 × 10 ¹⁰	73	D	0.18 ± 0.01	177.7 ± 0.4	T	
NGC4526	16.9 ± 1.6	-24.67 ± 0.20	43.8	0.63	111	2.8 ± 0.7 × 10 ¹⁰	205	L	
NGC4552	15.3 ± 1.0	-24.20 ± 0.14	25.4	0.08	150	2.3 ± 0.4 × 10 ¹⁰	40	O	0.05 ± 0.01	122.7 ± 1.5	W	
NGC4555	97.4 ± 14.6	-25.78 ± 0.33	10.9	0.16	125	5.1 ± 1.7 × 10 ¹⁰	
NGC4564	15.0 ± 1.2	-22.94 ± 0.17	19.9	0.54	50	6.8 ± 1.5 × 10 ⁹	155	D	0.53 ± 0.02	48.1 ± 0.3	W	
NGC4621	18.3 ± 1.7	-24.56 ± 0.20	32.9	0.37	165	2.9 ± 1.0 × 10 ¹⁰	140	D	0.35 ± 0.01	162.9 ± 0.1	W	
NGC4636	14.7 ± 0.9	-24.41 ± 0.13	59.3	0.22	148	2.7 ± 0.6 × 10 ¹⁰	30	M	0.17 ± 0.01	147.1 ± 0.6	V	
NGC4649	16.8 ± 1.2	-25.39 ± 0.15	45.2	0.19	110	5.9 ± 1.0 × 10 ¹⁰	110	D	0.18 ± 0.01	104.0 ± 0.4	V	
NGC4697	11.7 ± 0.8	-23.98 ± 0.14	42.4	0.33	65	1.7 ± 0.9 × 10 ¹⁰	110	P	0.45 ± 0.01	65.7 ± 0.4	T	
NGC5018	39.9 ± 6.0	-25.27 ± 0.33	15.6	0.28	95	6.3 ± 3.4 × 10 ¹⁰	65	Q	0.33 ± 0.01	93.8 ± 0.5	T	
NGC5044	31.2 ± 4.0	-24.76 ± 0.28	25.3	0.04	20	4.0 ± 1.8 × 10 ¹⁰	70	R	0.07 ± 0.01	3.1 ± 5.4	T	
NGC5102	4.0 ± 0.2	-21.09 ± 0.14	79.3	0.50	50	2.4 ± 0.4 × 10 ⁹	
NGC5171	99.3 ± 14.9	-24.95 ± 0.33	10.8	0.22	175	6.2 ± 2.0 × 10 ¹⁰	
NGC5532	104.5 ± 15.7	-26.33 ± 0.33	16.0	0.24	155	1.2 ± 0.5 × 10 ¹¹	
NGC5845	25.9 ± 2.5	-22.96 ± 0.21	4.9	0.32	140	5.3 ± 1.4 × 10 ⁹	110	S	0.28 ± 0.01	143.1 ± 0.3	W	
NGC5846	24.9 ± 2.3	-25.04 ± 0.20	34.5	0.06	30	4.4 ± 1.0 × 10 ¹⁰	< 10	R	0.05 ± 0.01	64.0 ± 1.9	W	
NGC6482	58.9 ± 8.8	-25.48 ± 0.33	12.6	0.28	65	1.1 ± 0.4 × 10 ¹¹	0.23 ± 0.01	66.8 ± 0.3	T	
NGC7052	70.2 ± 10.5	-25.66 ± 0.33	21.8	0.50	60	4.0 ± 1.2 × 10 ¹⁰	0.46 ± 0.01	63.5 ± 0.7	U	
NGC7618	77.2 ± 11.6	-25.40 ± 0.33	11.6	0.20	5	4.6 ± 2.2 × 10 ¹⁰	

^a Distances and associated errors in Mpc, taken from Tonry et al. (2001) and LEDA (Paturel et al. 1997), LEDA errors are assumed to be 15%.

^b Data taken from the 2MASS extended source catalog (Jarrett et al. 2000): absolute magnitude (K -band), half-light radius in $''$, effective ellipticity and position angle (all J -band).

^c Absolute blue luminosity in units of $L_{B,\odot} = 5.2 \times 10^{32} \text{ erg s}^{-1}$

^d Rotational velocities in km s^{-1} evaluated between $0.6 - 0.9 R_J$, taken from Hyperleda (Prugniel et al. 1998) references. A: Simien & Prugniel (1997a), B: Prugniel & Simien (1994), C: Bonfanti et al. (1995), D: Bender et al. (1994), E: D'Onofrio et al. (1995), F: Graham et al. (1998), G: Longo et al. (1994), H: Longhetti et al. (1998), I: Carollo & Danziger (1994b), J: Bettoni (1992), K: Fisher (1997), L: Pellegrini et al. (1997), M: Davies & Birkinshaw (1988), N: Simien & Prugniel (1998), O: Simien & Prugniel (1997b), P: Binney et al. (1990), Q: Carollo & Danziger (1994a), R: Carollo et al. (1993), S: Simien & Prugniel (2002).

^e Ellipticity and position angle, evaluated between $0.6 - 0.9 R_J$ from published optical surface photometry. T: Goudfrooij et al. (1994), U: Bender et al. (1988), V: Peletier et al. (1990), W: Falc3n-Barroso et al. (2006).

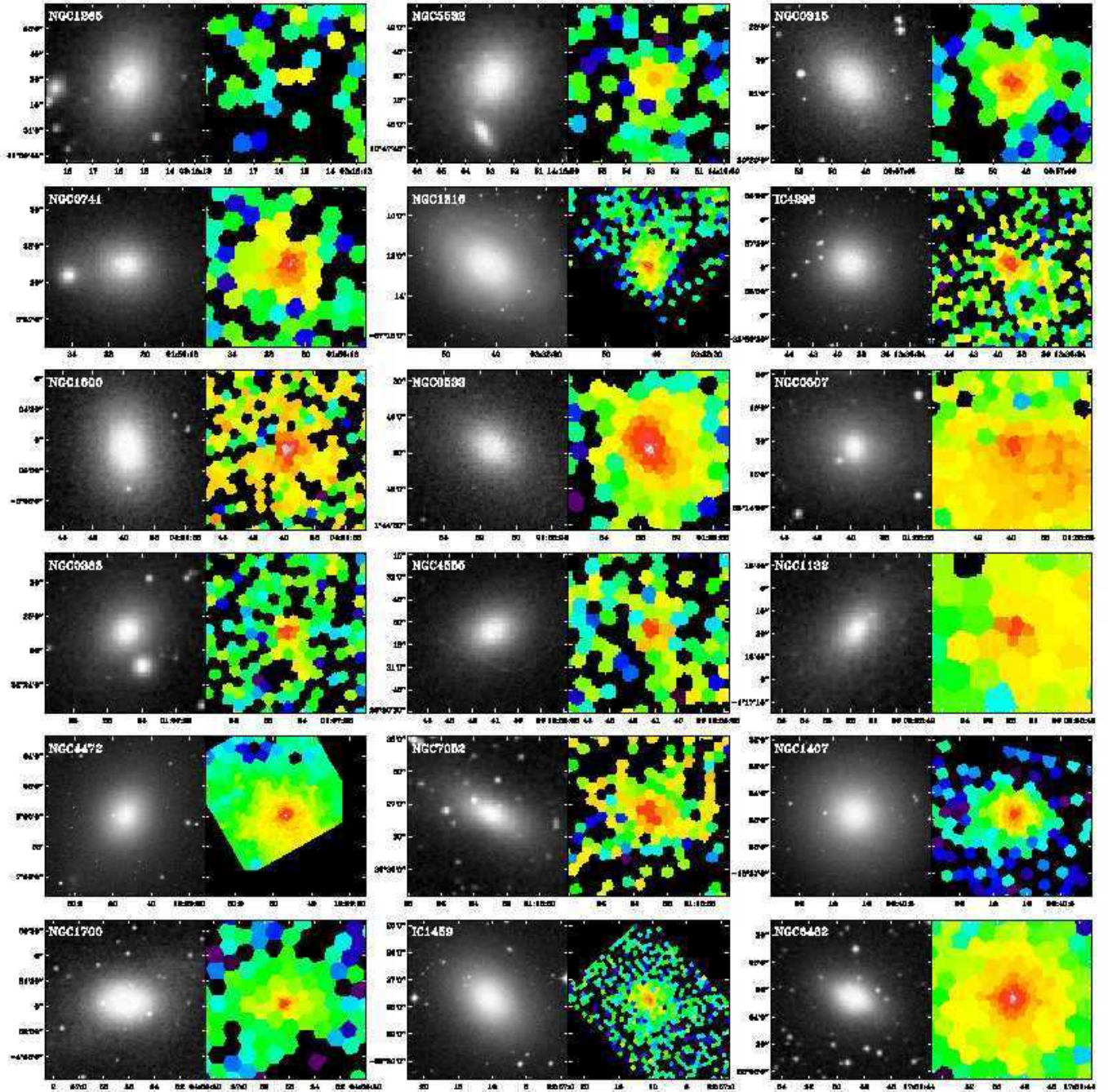


FIG. 2.— Adaptively binned *Chandra* X-ray gas surface brightness maps (right) and optical DSS *R*-band images (left). The objects are ordered by 2MASS *K* band luminosity, starting with the most luminous galaxy on the top left of the page, and decreasing to the right and then to the next row. The physical scale of each image is 50 kpc \times 50 kpc, except where indicated by an individually attached scale bar. The color range of the X-ray gas distribution is scaled logarithmically between 5×10^{-11} and 3×10^{-7} photons $\text{sec}^{-1} \text{cm}^{-2} \text{arcsec}^{-2}$. The *x* and *y*-axes are labelled according to right ascension and declination (2000), respectively.

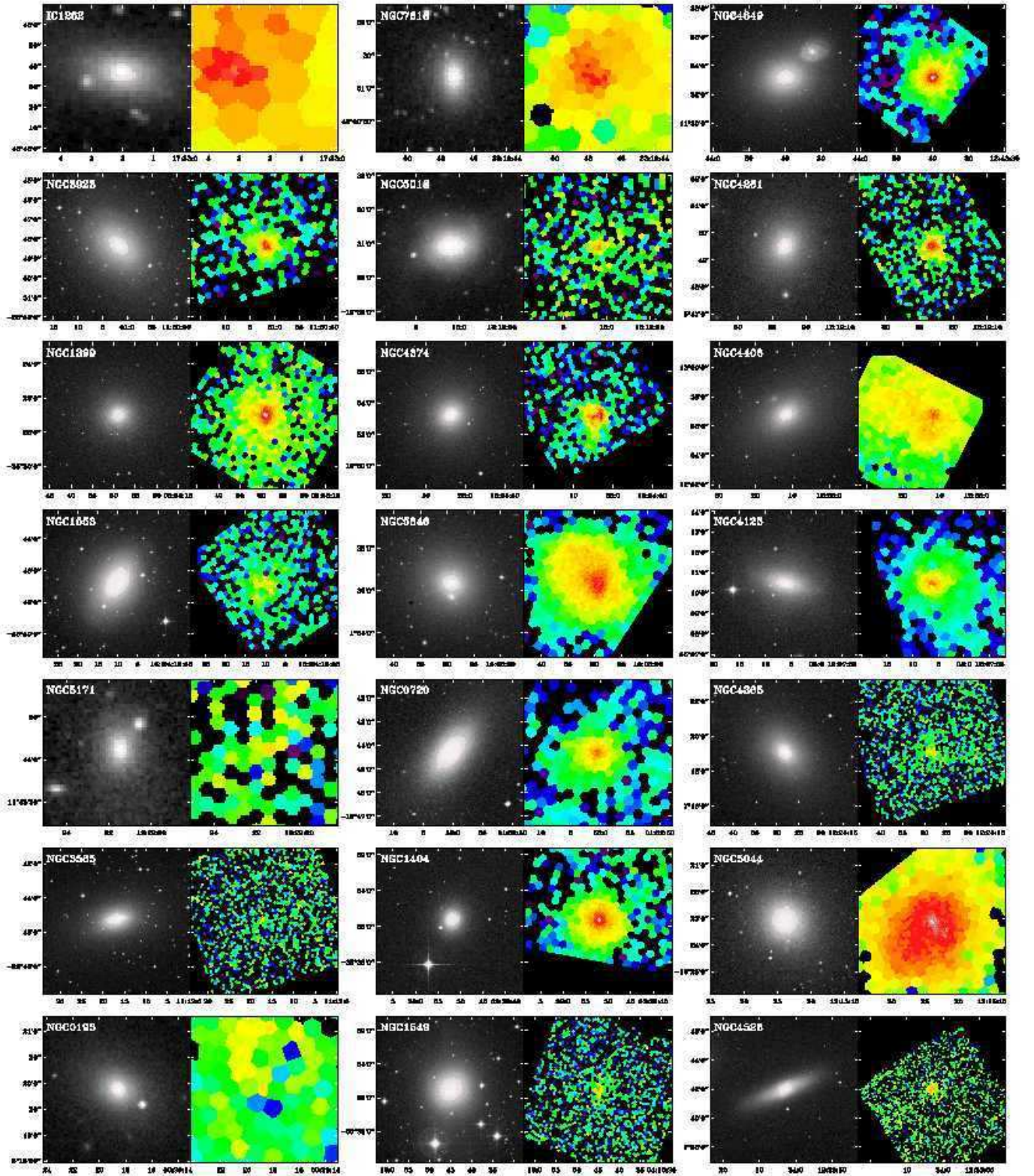


FIG. 2.— Continued

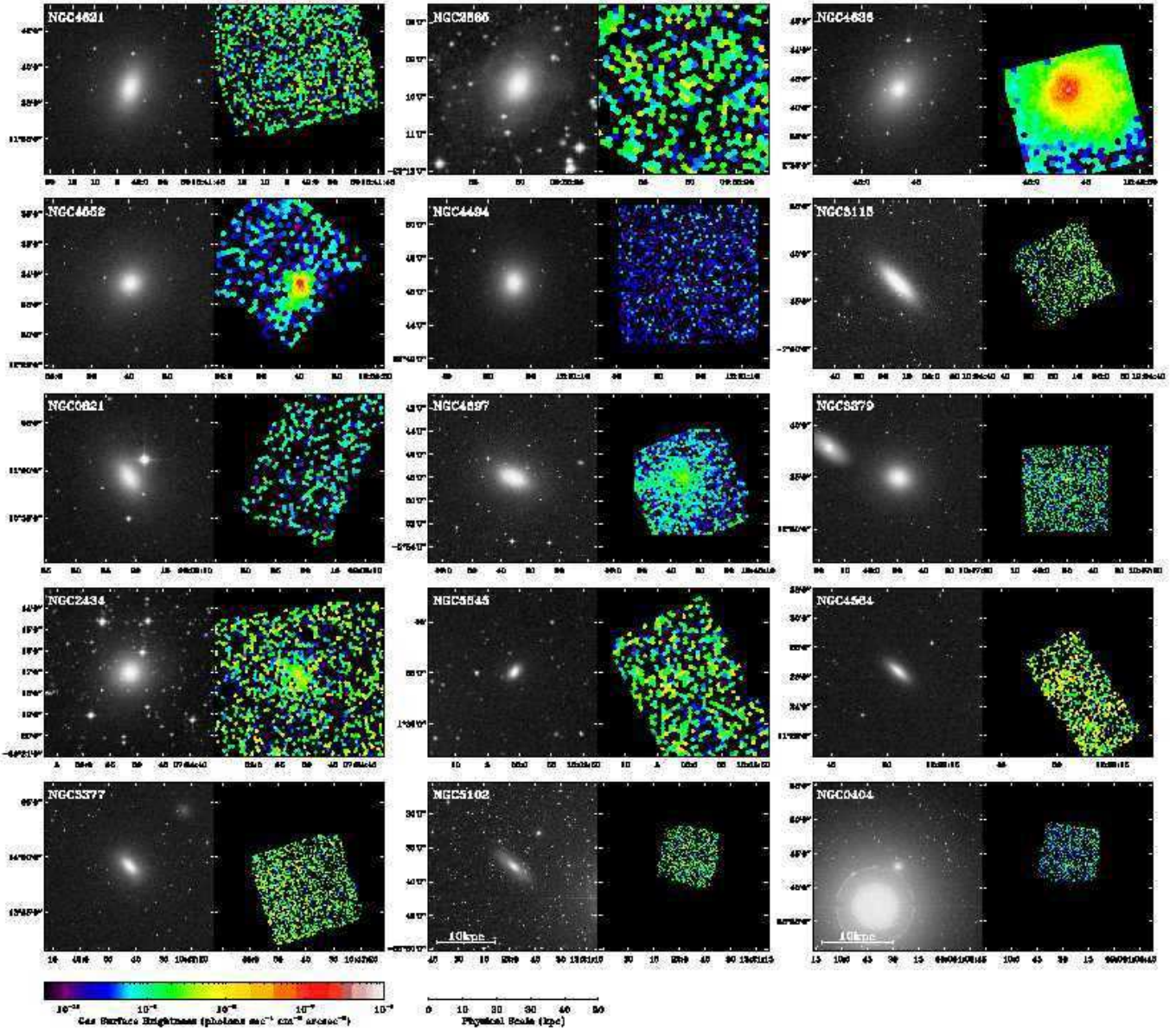


FIG. 2.— Continued

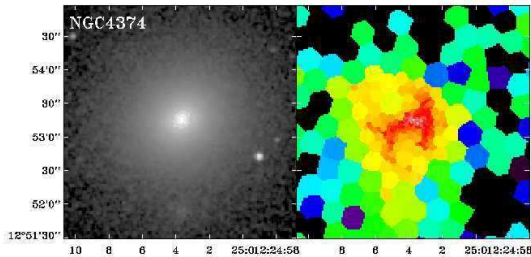


FIG. 3.— Adaptively binned *Chandra* X-ray gas surface brightness maps (right) and combined 2MASS *J*, *H* and *K_s*-band images (left). Figures 3a-ag showing all 33 galaxies with sufficient data to compute the X-ray ellipticity ϵ_X are available in high-resolution in the electronic edition of the Journal. The printed edition contains only a sample (NGC 4374). When available, 2MASS images were taken from the 2MASS Large Galaxy Atlas (Jarrett et al. 2003, <http://irsa.ipac.caltech.edu/applications/2MASS/LGA/atlas.html>), otherwise images are taken from the 2MASS Extended Source Catalog (Jarrett et al. 2000). The physical scale of each image is $6R_J$ across. The color range of the X-ray gas distribution is scaled logarithmically between 5×10^{-11} and 1×10^{-6} photons $\text{sec}^{-1} \text{cm}^{-2} \text{arcsec}^{-2}$, and is identical to that of Figure 2. The x and y-axes are labelled according to right ascension and declination (2000), respectively.

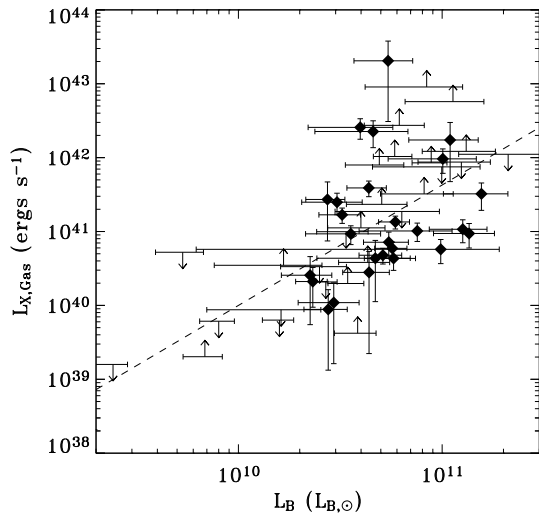


FIG. 4.— Total X-ray gas luminosity in ergs s^{-1} as a function of absolute blue luminosity in units of blue solar luminosity ($L_{B,\odot} = 5.2 \times 10^{32} \text{ ergs s}^{-1}$) taken from LEDA. The dashed line shows the best fit by O’Sullivan et al. (2001), which they statistically correct for the expected contribution from unresolved point sources. Our data are consistent with their relation.

ter is not caused by systems with obviously disturbed X-ray morphology. Of the 8 most highly disturbed systems (quantified by the asymmetry index defined in Paper II), 6 do not have published optical surface photometry, and are not plotted in Figure 6; removing the remaining two (NGC 4374 and NGC 5044) makes an insignificant difference. Excluding group member galaxies, or systems with significant optical isophotal twists or ellipticity gradients also has negligible effect.

This lack of correlation is very surprising if hydrostatic equilibrium holds precisely. Roughly speaking, if one assumes an oblate logarithmic potential, the equipotential surfaces should be about one third as flattened as the underlying density distribution (Binney & Tremaine 1987). Instead, we find that the X-ray isophotes are often much flatter than the stellar isophotes. We fully discuss the

implications of this result, with detailed modeling, in § 4.1 below.

We notice a weak tendency for galaxies to have their X-ray gas major axis aligned with the stellar distribution. Given the fact that X-ray isophotal twists often correlate with the orientation of asymmetries in the gas, it is not clear whether this alignment is a consequence of the underlying potential. An alternative is that it is a consequence of a misalignment between radio sources optical major axes (Palimaka et al. 1979), which is present in our sample and which we fully discuss in Paper II.

3.3. Rotational Support

A significant fraction of the hot gas in elliptical galaxies is believed to be due to stellar mass-loss (e.g. Brighenti & Mathews 2000). Thus, the gas should contain a significant amount of specific angular momentum, causing it to settle into a flattened rotating disk (Brighenti & Mathews 1997). This scenario predicts a relationship between the stellar rotational velocity and the X-ray gas ellipticity, with faster rotating systems exhibiting flatter gas isophotes. Figure 7 shows the observed X-ray ellipticity between 0.6 and $0.9R_J$ as a function of mean stellar rotational velocity in the same radial range. In agreement with previous ROSAT and Einstein observations of elliptical galaxies (Hanlan & Bregman 2000), we find no evidence for any correlation between these parameters. A Spearman rank analysis yields a probability of 54% for the null hypothesis of no correlation. While this is formally an upper bound on the probability due the presence of finite measurement errors and the presence of upper limits, it is obvious from the figure that the errors are not responsible for the absence of correlation.

Such a lack of correlation could still be consistent with an alternative scenario, where the majority of the hot gas is not due to stellar mass loss, but instead is acquired externally through mergers, infalling gas clouds or through tidal stripping during close encounters. The hot gas would then slowly flow toward the center and settle into a cooling disk (e.g. Brighenti & Mathews 1997). Thus, if angular momentum is conserved during the inflow, one should be able to observe a trend for the X-ray ellipticities to rise inward (Hanlan & Bregman 2000), as the angular momentum becomes more important. The detailed ellipticity profiles in Figure 5 do not support this prediction observationally, since ellipticities do not systematically increase inward. Moreover, significant rotational support would not account for the prevalence of strong isophotal twists.

4. DISCUSSION

4.1. Implications for Hydrostatic Equilibrium

Within one stellar effective radius, the gravitational potentials of normal elliptical galaxies are dominated by the stellar component. Although some studies have found dark matter contributions in individual objects as high as 40% within this radius (Gerhard et al. 2001; Padmanabhan et al. 2004), in general the dark matter halo contribution should be secondary (e.g. Mamon & Lokas 2005). Thus, if the assumption of hydrostatic equilibrium were valid, one would expect the hot gas isophotes to reflect the shape of the stellar po-

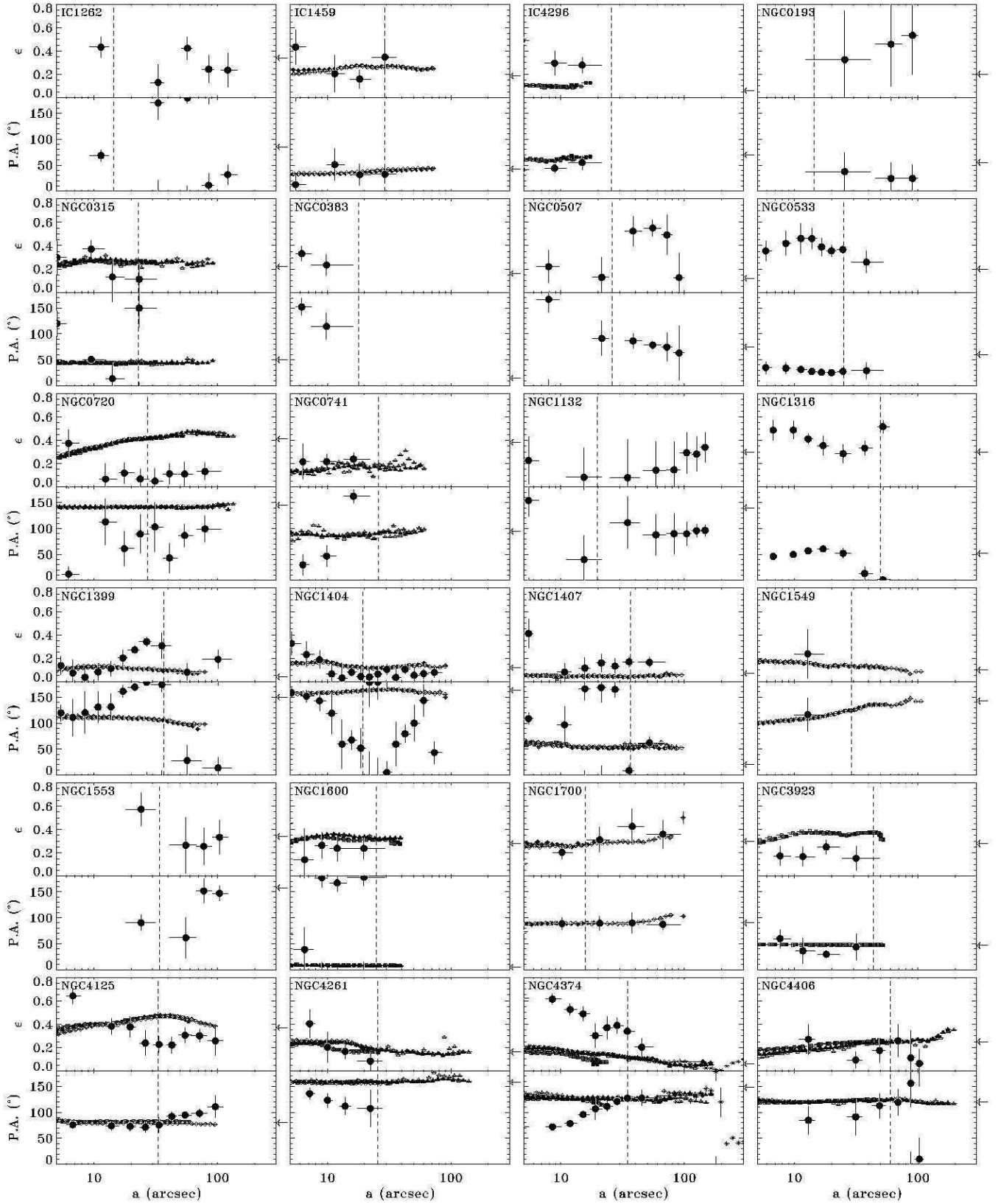


FIG. 5.— Radial isophotal ellipticity and position angle profiles for the subset of 36 elliptical galaxies containing sufficient signal. Large filled circles with error bars denote X-ray gas profiles; other symbols denote optical profiles as indicated in the figure. The 2MASS ellipticity and position angle are marked with arrows at the right border. The vertical dashed lines mark the 2MASS *J*-band effective radius.

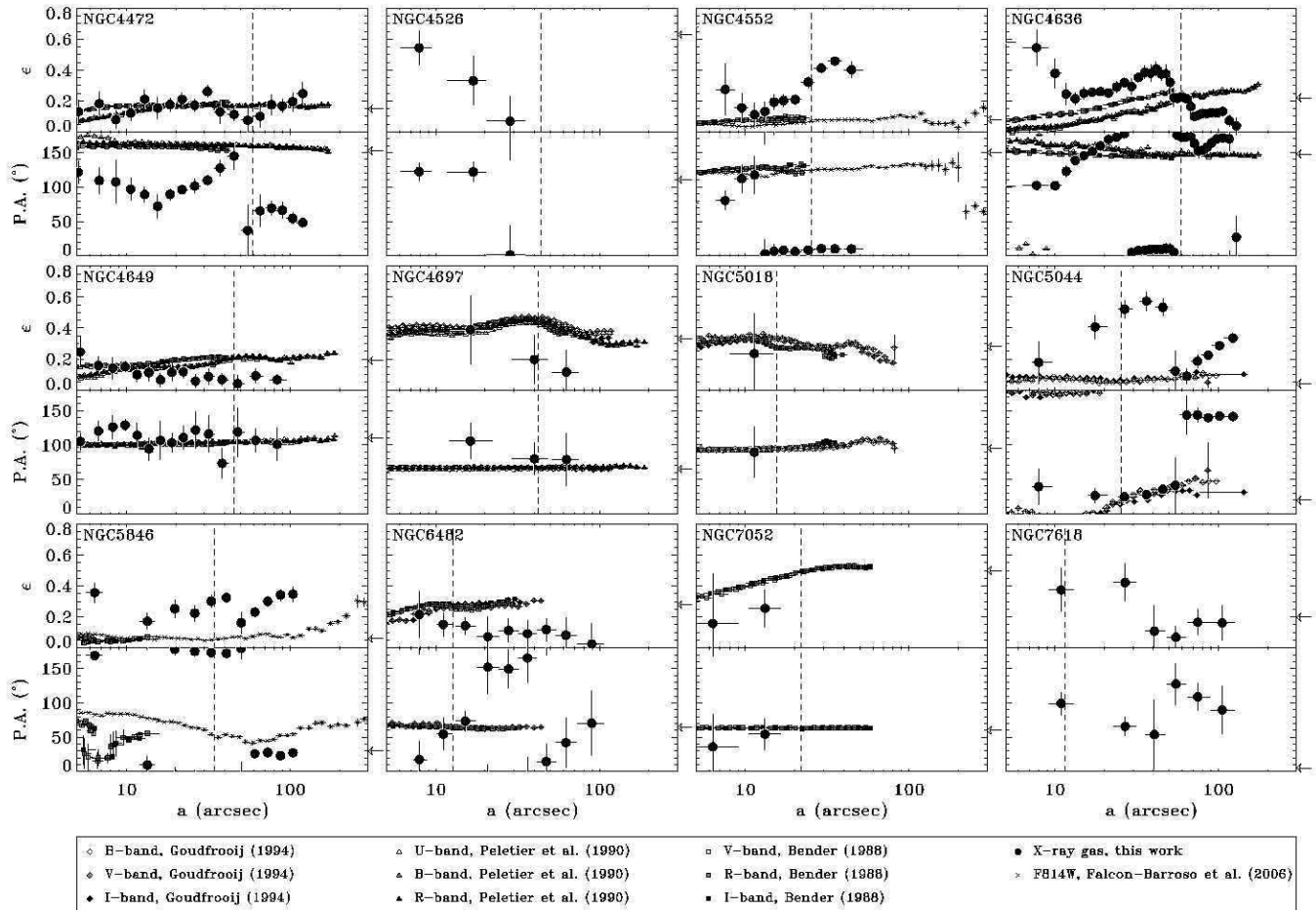


FIG. 5.— Continued.

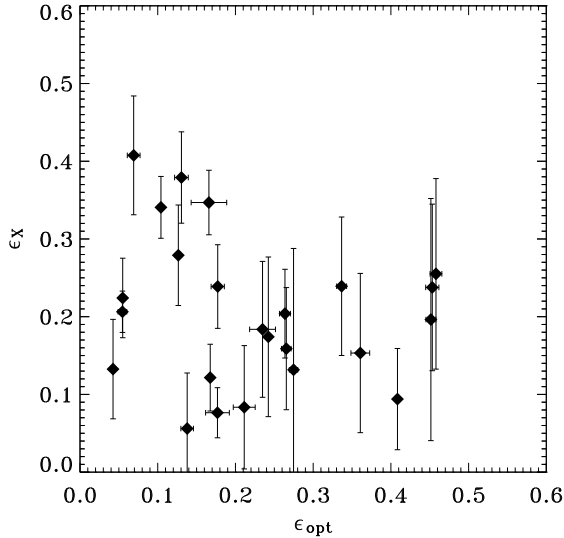


FIG. 6.— X-ray gas ellipticity vs. optical ellipticity, both evaluated between $0.6 - 0.9 R_J$. There is no correlation, contrary to what would be expected if the gas were in hydrostatic equilibrium in a stellar-mass-dominated potential. See also Figure 8 for theoretical predictions.

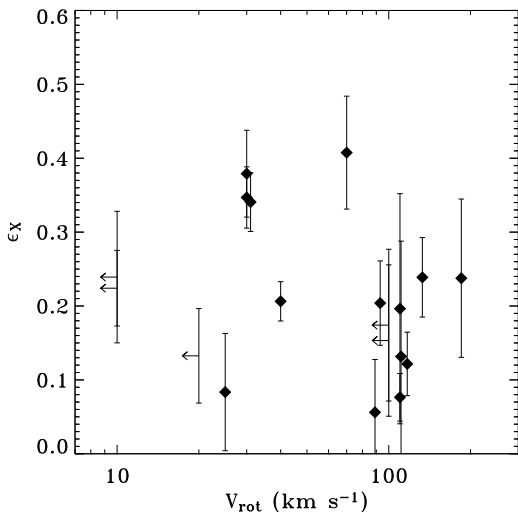


FIG. 7.— X-ray ellipticity as a function of rotational stellar velocity between $0.6 - 0.9 R_J$. No correlation is present, contrary to what is expected if the hot gas would be due to stellar mass-loss and subsequently settle into a cooling disk.

tential (Buote & Canizares 1994). Since projected isopotentials are rounder than the projected isopleths of the underlying density, we would also expect the gas emission to be rounder than the starlight. However, Figure 6 shows that the gas is flatter than the starlight in one-third of the sample, and that gas and optical ellipticities are completely uncorrelated. In fact, the Spearman rank-order correlation coefficient is slightly negative, with a value of -0.191 . A two-sided confidence test shows that the difference from zero is not statistically significant.¹⁰

To determine whether the gas may still be hydrostatic despite being morphologically uncorrelated with the starlight, we simulate hydrostatic systems in a va-

riety of stellar-plus-dark-matter potentials. The stellar component is represented by a triaxial Hernquist model, whose mass density is given by

$$\rho_* = \frac{\rho_H}{(a/a_*)(1 + a/a_*)^3}, \quad (4)$$

where a is the semimajor axis of the ellipsoidal equidensity surface, a_* is the scale length, and ρ_H is a normalization constant. The dark halo is taken to be either a triaxial NFW model, having density

$$\rho_{\text{DM}} = \frac{\rho_{\text{NFW}}}{(a/a_{\text{DM}})(1 + a/a_{\text{DM}})^2}, \quad (5)$$

or a similar profile with a flat core:

$$\rho_{\text{DM}} = \frac{\rho'_{\text{NFW}}}{(1 + a/a_{\text{DM}})^3}. \quad (6)$$

We parametrize the models by the short-to-long axis ratio c/a and triaxiality $T = (a^2 - b^2)/(a^2 - c^2)$ of the stellar and dark matter components, the ratio of scale lengths $\bar{a} \equiv a_{\text{DM}}/a_*$, and the ratio \bar{M} of dark to luminous mass inside the half-mass radius of the stellar component.¹¹ The potentials are computed using the formulae in the appendix of Flores et al. (2005).

The principal axes of the two components are assumed to be aligned and not intrinsically twisted. We do not consider misaligned or twisted models because there are no self-consistent equilibrium models for such configurations. Intrinsically misaligned or twisted galaxies, if they exist, would likely be in some normal mode of oscillation whose period is of order the dynamical time, and so any gas in these systems would not be hydrostatic. We also do not consider stellar distributions with radially varying axis ratios. Even though this would tend to slightly decouple the local ellipticities of the starlight and the stellar potential, this is a moot point. Only two objects in Figure 6 show significant ellipticity gradients, and the results are unchanged if these are removed.

The *a priori* axis ratio distribution of the stellar components is chosen to be approximately consistent with the observed ellipticity distribution of normal ellipticals. For populations of purely oblate or purely prolate systems, we use rough analytic fits to the distributions obtained by Vincent & Ryden (2005) from the Sloan Digital Sky Survey Data Release 3. It is well known (Ryden 1996; Tremblay & Merritt 1995) that purely axisymmetric populations cannot reproduce the observed ellipticity distribution without invoking negative numbers of galaxies. We force our fits to be strictly positive, even though this means that the observed ellipticity distribution is not exactly recovered. For triaxial populations we use an analytic fit to the “maximal ignorance” distribution of Bak & Statler (2000). This distribution is derived from simultaneous fits to surface photometry and stellar kinematics for 13 galaxies, and is consistent with the overall ellipticity distribution.

The combined potential is filled with isothermal gas, at a temperature that mimics the typical observed surface brightness profiles. We orient the system at random, and

¹⁰ This statement also holds for extraction annuli ranging between 0.5 and $1.2 R_J$, as well as for the sample with the disturbed objects removed.

¹¹ The half-mass radius of the Hernquist model is $(1 + 2^{1/2}) a_*$, the semimajor axis of the isodensity surface containing half the mass.

project the X-ray emissivity, which we take to be proportional to the square of the gas density. We calculate the stellar and gas isophotal ellipticities at 0.75 of the stellar effective radius,¹² to correspond with Figure 6. The results are quite insensitive to the assumed temperature; we are therefore confident that they will apply to moderately non-isothermal equations of state as well.

We first compute models in which the shapes of the dark halos are correlated with the shapes of the stellar components. The latter are taken to be triaxial, drawn from the Bak & Statler (2000) distribution. For each object, the halo triaxiality T and axis ratio c/a are chosen randomly from a gaussian distribution centered on the stellar values, with a width σ . We consider strongly ($\sigma = 0.2$) and weakly ($\sigma = 0.4$) correlated halos. We compute an ensemble of several hundred models, oriented at random, to define the predicted distribution in the ϵ_X - ϵ_{opt} plane. Examples for strongly and weakly correlated halos are shown in Figure 8a and 8b. Not surprisingly, these models predict a significant correlation between ϵ_X and ϵ_{opt} .

To assess quantitatively whether the models can be consistent with the observed distribution, we create several thousand simulated 24-object samples. For each simulated sample, we randomly perturb the ϵ_X and ϵ_{opt} values according to the actual measurement errors in the observed sample. We then compute the Spearman rank-order correlation coefficient and the unweighted mean ellipticity ($\langle \epsilon_X \rangle$), and determine the joint probability that the model will produce a Spearman coefficient as low as, and a mean ellipticity as high as, the observed values. In assessing the models we consider \bar{M} values of 0.1, 0.3, 1, 3, and 10, and \bar{a} values of 1, 3, and 10.

We find that all of the correlated halo models are ruled out at $> 99.9\%$ confidence. This is the case even if dark mass exceeds stellar mass by as much as a factor of 10 inside the stellar half-mass radius. Clearly, if the isophotal ellipticity of hydrostatic gas is to be uncorrelated with that of the starlight, the shape of the halo must be uncorrelated with that of the stars.

Accordingly, we next consider a variety of uncorrelated halo models. These come in two types: (1) triaxial stellar components with either purely oblate or purely prolate halos having flattenings c/a of 0.5 and 0.2; and (2) axisymmetric (oblate or prolate) stellar components with random triaxial halos. Examples are shown in Figure 8c-f. Here we find that all of the following are excluded at $\geq 99\%$ confidence: (1) oblate halos; (2) random triaxial halos with mass ratios $\bar{M} \leq 3$; (3) prolate halos with $c/a = 0.5$ and $\bar{M} < 3$; and (4) prolate halos with $c/a = 0.2$ and $\bar{M} < 0.3$.

This result does not rely on the presence of a large number of clearly disturbed objects in the sample. Six of the eight most asymmetric systems are not represented in Figure 6 because they do not have published optical surface photometry. Nonetheless, the objects with the largest ϵ_X values in Figure 6 are NGC 4374 and NGC 5044. Of these, the former is clearly disturbed by its radio source, and the latter is lopsided at large radius, suggesting an interaction with the intergalactic medium.

If we cull these two objects from the sample, the constraints are weakened slightly but our qualitative result still holds. Correlated halo models are still ruled out at $> 99.9\%$ confidence, and random triaxial halos with mass ratios $\bar{M} \leq 3$ are still excluded at 99% confidence. Oblate halos are excluded at 97% confidence, and prolate halos with $c/a = 0.5$ and $\bar{M} < 3$ are excluded at 98% confidence. Prolate halos with $c/a = 0.2$ cannot be excluded for $\bar{M} \geq 0.1$.

Thus the only viable hydrostatic models are those in which the shape of the halo has nothing to do with the shape of the luminous galaxy; moreover, the dark halo must either dominate over luminous matter inside the stellar half-mass radius or be prominently sausage- or cigar-shaped. Both of these options conflict with well established results. There is widespread agreement, from stellar population modeling coupled with stellar dynamics or X-ray data, that normal ellipticals are not dark-matter-dominated in the inner 1 effective radius (Loewenstein & White 1999; Mamon & Lokas 2005; Lintott et al. 2006; Humphrey & Buote 2006). The mass fractions obtained in these studies correspond to $0.2 < \bar{M} < 1.0$, which are ruled out by our simulations except for the case of flat, prolate halos. But numerous simulations of galaxy mergers and structure formation (Barnes & Hernquist 1996; Sugerma et al. 2000; Meza et al. 2003; Bailin & Steinmetz 2005; Allgood et al. 2006; Cox et al. 2006) demonstrate that halos should be neither prolate nor highly flattened. Moreover, there is no compelling reason to expect that dark and stellar matter distributions should have very different shapes; both obey the same collisionless dynamics, and should end up similarly distributed following a major event such as a merger. We are therefore forced to the conclusion that the assumption of hydrostatic equilibrium must be incorrect.

To be more precise, even though the gas in normal ellipticals may be, on average, close enough to hydrostatic that reasonable radial mass profiles can be derived, hydrostatic equilibrium does not hold tightly enough that X-ray morphology can be used to trace the shape of the total mass distribution. Buote and collaborators (Buote et al. 2002; Buote & Canizares 1996, 1994) have used this technique to argue for a flattened dark matter halo in NGC 720. While it is possible that hydrostatic equilibrium could hold in some individual systems, our results show that this would be the exception rather than the rule, and there is no independent test to reveal where hydrostatic equilibrium does hold. Also, in the case of NGC 720, we find that properly removing the resolved and unresolved LMXB emission reduces the gas ellipticity, and, along with it, the need for a flattened dark halo. The ϵ_X profile we show in Figure 5 appears to be entirely consistent with the oblate mass-follows-light model of Buote et al. (2002, Fig. 3) at radii between $10''$ and $80''$. However, a direct comparison is complicated by the fact that Buote et al. (2002) do not measure *isophotal* ellipticities and position angles, but rather their mean values *inside* elliptical apertures.¹³

To preserve hydrostatic equilibrium in the general

¹² The effective radius is the semimajor axis of the isophote enclosing half the projected light, which depends on the axis ratios and viewing geometry.

¹³ The mass-follows-light model does not reproduce the offset between optical and X-ray position angles, a failing that does not have a unique interpretation.

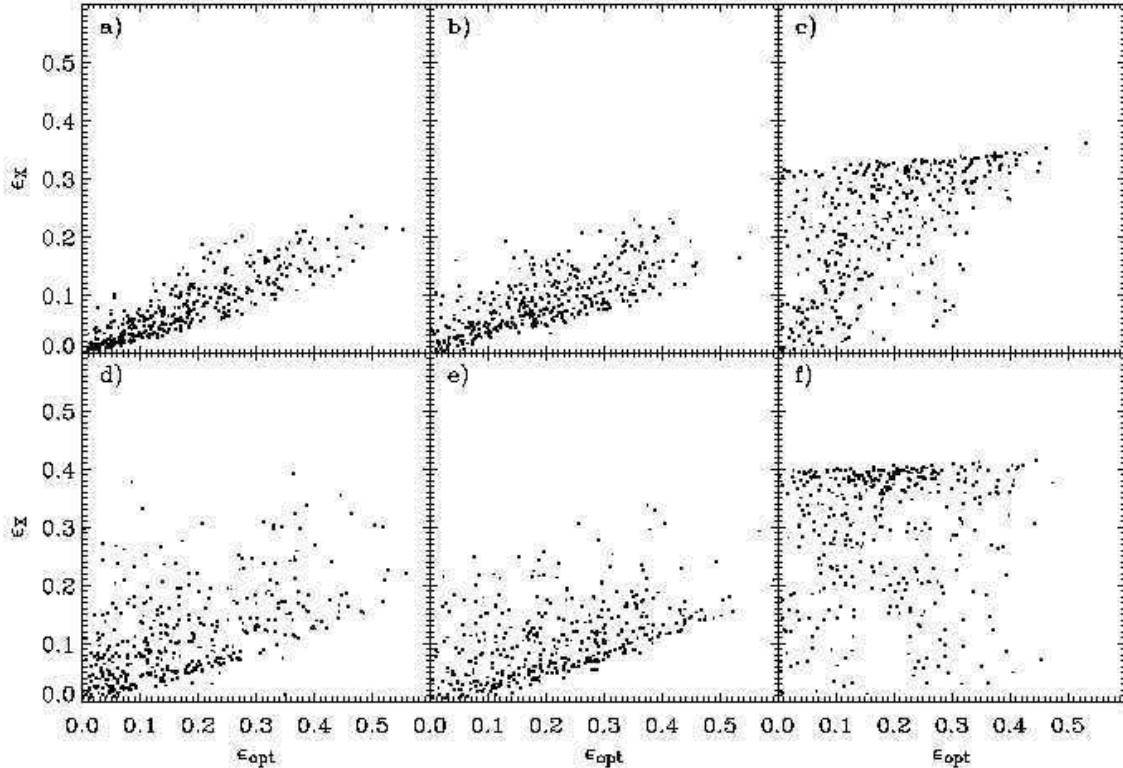


FIG. 8.— Examples of predicted intrinsic (i.e., not convolved with measurement errors) distributions in the $\epsilon_X - \epsilon_{\text{opt}}$ plane for isothermal gas in model stellar-plus-dark-matter potentials. (a,b) Triaxial stellar components with (a) strongly and (b) weakly correlated halos (see § 4.1); (c) triaxial stellar components with oblate halos of flattening $c/a = 0.2$; (d) oblate and (e) prolate stellar components with random triaxial halos; (f) triaxial stellar components with prolate halos of flattening $c/a = 0.2$. Examples shown here all have equal contributions of dark and stellar matter ($\bar{M} = 1$) and $\bar{a} = 3$. Panels (a), (b), (e), and (f) are computed for NFW halos (equation 5); panels (c) and (d) use the flat-core halos (equation 6).

population of ellipticals, our data would require extremely flat, complex dark matter halos with significant substructure to explain the large ellipticities and isophotal twists. This is highly unlikely and inconsistent with stellar kinematics (e.g. Cappellari et al. 2006) or simulations of large-scale structure formation (e.g. Springel et al. 2005). Even though triaxial dark matter halos are able to produce simple twists in X-ray isophotes (Romanowsky & Kochanek 1998), these effects would be insufficient to explain the complexity and magnitude of the observed features.

We see no delineation between disturbed systems that are not hydrostatic and undisturbed systems that are. While we cannot prove that the round, symmetric systems are not hydrostatic, we emphasize that the sample, as a whole, has failed the test. If one chooses to invoke hydrostatic equilibrium for a system that appears “relaxed,” it should be clearly understood that this reflects a hope rather than a verifiable assumption.

We take the view that the isophotal ellipticity of the X-ray gas does not reflect the underlying potential. Ellipticity is merely a measure of the $m = 2$ Fourier amplitude of the deviations from circular symmetry. In the optical, the other Fourier harmonics are small by comparison; in the X-ray, they are not. In Paper II of this series we will argue that the gas ellipticity is a measure of morphological disturbance, quantify that disturbance, and demonstrate that it is likely produced by AGN.

The assumption of hydrostatic equilibrium is widely used to derive radial mass profiles (e.g. Forman et al.

1985; Killeen & Bicknell 1988; Paolillo et al. 2003; Humphrey et al. 2006; Fukazawa et al. 2006). If the gas is not hydrostatic, what are the consequences? Imagine a region that was locally overpressured by a factor q . Assuming adiabatic expansion this region would expand by a factor $q^{1/5}$ in linear size over a sound crossing time scale of $\sim 10^8$ years, to regain pressure equilibrium. To redistribute gas a significant distance along an equipotential would thus imply an overpressure $q \lesssim 10$. If the galaxy were *globally* overpressured by this factor, one would infer a mass a factor of q too large. However, normal ellipticals are probably only locally overpressured, and so averaging azimuthally over N over- and underpressured regions in a radial analysis would tend to reduce this effect by a factor of order $N^{1/2}$, resulting in a mass estimate in error by at most a factor of a few, either high or low. Subsonic bulk motions generated by such temporary overpressures could also enhance or reduce radial pressure support, depending on their radial gradient.

An early study by Schindler (1996) demonstrated that mass profiles of simulated clusters can be recovered successfully with the hydrostatic equilibrium method, limited primarily by the presence of significant substructure. More recent studies of hydrodynamic cluster formation simulations (Rasia et al. 2004; Nagai et al. 2007) show that neglecting bulk motion in a hydrostatic analysis tends to underestimate the gravitating mass by 5 to 20%. Rasia et al. (2006) find a further systematic effect of similar magnitude that they attribute to the complex temperature structure of the cluster; however this ap-

pears only when they reduce the backgrounds in their simulated observations far below typical *Chandra* values. Unfortunately, no such study is available for the mass regime of normal elliptical galaxies and none yet takes into account disturbances due to AGN activity, which our simple arguments above suggest may be larger in magnitude. On the observational side, Fukazawa et al. (2006) derive total mass profiles from *Chandra* X-ray data of 53 normal elliptical galaxies assuming hydrostatic equilibrium and compare 7 of these to mass profiles based on stellar kinematics. They find that for 2 out of 7 galaxies, total enclosed masses (inside observationally accessible maximum radii) differ by a factor of ~ 2 and for one object, NGC 3379, the difference even grows to a factor of ~ 7 . Pellegrini & Ciotti (2006) reconcile this discrepancy for NGC 3379 by fitting its X-ray properties with a wind model, staying consistent with the optically derived mass profile. They conclude that the gas is not in hydrostatic equilibrium, but in a general state of outflow, calling the X-ray mass measurement into question.

4.2. Implications for Rotational Support

The hot gas in elliptical galaxies is believed to come from some combination of stellar mass loss, infall or mergers. In each case, the gas should carry significant amounts of angular momentum. In a standard cooling flow model that conserves angular momentum, the gas will settle into rotationally supported cooling disks (Brighenti & Mathews 1997, 1996; Kley & Mathews 1995). These rotating cooling flow models predict ellipticity profiles that rise inward, with minimal isophotal twist.

Figures 5 and 7 show that these predictions are inconsistent with observations. Although we do find rather large X-ray ellipticities, they do not systematically increase toward smaller radii. Our profiles also reveal dramatic isophotal twists and asymmetries that would not arise naturally in a scenario where the ellipticities are caused by rotation alone. In addition, we find no relation between stellar rotational velocity and the gas flattening, as one would expect if the gas is mainly due to stellar mass loss. Thus, we conclude that the X-ray gas morphology is not dictated by rotation, in agreement with previous ROSAT observations (Hanlan & Bregman 2000).

The question now is whether the failure to observe rotationally flattened X-ray disks is a serious blow to cooling flow models. One way to save the cooling flow picture would be to efficiently transfer angular momentum through turbulence in the gas (Shadmehri & Ghanbari 2002; Brighenti & Mathews 2000), but it is unclear how effective this process is for elliptical galaxies. Another alternative is that spatially distributed multi-temperature mass dropout can circularize the X-ray isophotes (Hanlan & Bregman 2000). However, recent XMM-Newton spectroscopy of normal elliptical galaxies (e.g. Xu et al. 2002; Buote et al. 2003) rules out the existence of sufficient intermediate temperature gas. In addition, Bregman et al. (2006) are able to directly trace the amount of this intermediate gas by measuring its O VI emission ($\sim 10^{5.5}\text{K}$) with the *Far Ultraviolet Spectral Explorer* (FUSE). Bregman et al. (2005) examine the spatial distribution of this warm gas for NGC 4636 and NGC 5846 and constrain the size of the cooling region to

be smaller than 0.8 kpc and 0.5 kpc, respectively. Their measurements are consistent with moderate cooling flows with centrally concentrated mass dropout and rule out spatially distributed dropout for these galaxies.

Another explanation for the lack of disk signatures is that the hot gas is actually flowing outward instead of inward, eliminating the need for the gas to settle into a cooling disk. An idea by Brighenti & Mathews (2006) seems to be successful in stopping inward cooling flows by AGN-induced massive jet outflows, which are stable for several gigayears.

Alternatively, morphological asymmetries, which are clearly significant, may be masking possible disk signatures. Whatever the cause of these asymmetries (see Paper II), this effect could be effective in disrupting the flattest X-ray isophotes at small radii close to the center. Detailed simulations are needed to confirm this possibility. Thus, our results do not imply that rotational support of the hot gas in elliptical galaxies has no importance at all. We can merely state that it is not the *dominant* factor that causes the large observed ellipticities.

There is other evidence that gas rotation might be present. For example, Statler & McNamara (2002) find extremely flat X-ray emission in NGC 1700, which they interpret as a large-scale cooling disk. Their model yields a specific angular momentum and cooling time for the hot gas that is consistent with the gas having been acquired during the last major merger. We find that removal of unresolved point sources somewhat reduces the X-ray ellipticity of this object; but the data are still consistent with their claimed 15 kpc rotating disk. Additional support for rotation has recently been reported by Bregman et al. (2005), who find that the O VI line structure of NGC 4636 exhibits signs consistent with rotation.

5. CONCLUSIONS

We have analyzed the X-ray emission of 54 normal elliptical galaxies in the *Chandra* archive and isolated their diffuse hot interstellar gas emission from the emission of discrete stellar point sources for the first time. We qualitatively and quantitatively compare the morphology of the hot gas to the shape of the stellar distribution and find that they have very little in common, despite the known L_X-L_B relation. We compute ellipticity and position angle profiles for the X-ray gas and compare them to published optical profiles. In particular, we do not find a correlation between optical and X-ray ellipticities measured in the regions where stellar mass dominates the potential, suggesting that the gas is at least far enough out of hydrostatic equilibrium that the information about the shape of the underlying potential is lost. We also argue that X-ray derived radial mass profiles may be in error by factors of as much as a few, without the necessity for the galaxy to drive a global wind.

Although we find large X-ray gas ellipticities to be common, the gas morphology is generally inconsistent with rotationally flattened disks, and a comparison with stellar rotational velocities yields no evidence for significant rotational support.

The fact that neither the shape of the underlying potential nor rotational support determine the overall distribution of the X-ray emitting gas, combined with its general disturbed appearance, suggests the involvement

of another major component: the central AGN. We assess the importance of the AGN in Paper II, where we draw a connection between gas morphology and AGN luminosity. These new findings are consistent with the AGN constantly stirring up the interstellar medium by inflating buoyant bubbles, which may also play a role in redistributing the angular momentum of the hot gas through entrainment. These intermittent AGN outbursts could also be responsible for disrupting or masking the signatures of cooling disks in the central regions of elliptical galaxies.

We would like to thank Jesus Falc3n-Barroso and the SAURON team for allowing us to use their yet unpublished MDM photometry. We have made use of the HyperLEDA database (<http://leda.univ-lyon1.fr>) and of data products from the Two Micron All Sky Survey, which is a joint project of the University of Massachusetts and the Infrared Processing and Analysis Center/California Institute of Technology, funded by the National Aeronautics and Space Administration and the National Science Foundation.

We also made use of the Digitized Sky Surveys which were produced at the Space Telescope Science Institute under U.S. Government grant NAG W-2166. The “Second Epoch Survey” of the southern sky was produced by the Anglo-Australian Observatory (AAO) using the UK Schmidt Telescope. The digitized images are copy-

right (c) 1993-1995 by the Anglo-Australian Telescope Board, and are distributed herein by agreement. The “Equatorial Red Atlas” of the southern sky was produced using the UK Schmidt Telescope. Plates from both surveys have been digitized and compressed by the ST ScI. The digitized images are copyright (c) 1992-1995, jointly by the UK SERC/PPARC (Particle Physics and Astronomy Research Council, formerly Science and Engineering Research Council) and the Anglo-Australian Telescope Board, and are distributed herein by agreement. All Rights Reserved. The compressed files of the “Palomar Observatory - Space Telescope Science Institute Digital Sky Survey” of the northern sky, based on scans of the Second Palomar Sky Survey, are copyright (c) 1993-1995 by the California Institute of Technology and are distributed herein by agreement. All Rights Reserved.

Support for this work was provided by the National Aeronautics and Space Administration (NASA) through Chandra Awards G01-2094X and AR3-4011X, issued by the *Chandra X-Ray Observatory Center*, which is operated by the Smithsonian Astrophysical Observatory for and on behalf of NASA under contract NAS8-39073, and by National Science Foundation grant AST0407152. Any opinions, findings, and conclusions or recommendations expressed in this material are those of the authors and do not necessarily reflect the views of the National Science Foundation.

REFERENCES

- Allgood, B., Flores, R. A., Primack, J. R., Kravtsov, A. V., Wechsler, R. H., Faltenbacher, A., & Bullock, J. S. 2006, *MNRAS*, 367, 1781
- Bailin, J., & Steinmetz, M. 2005, *ApJ*, 627, 647
- Bak, J., & Statler, T. S. 2000, *AJ*, 120, 110
- Barnes, J. E., & Hernquist, L. 1996, *ApJ*, 471, 115
- Bender, R., Doebereiner, S., & Moellenhoff, C. 1988, *A&AS*, 74, 385
- Bender, R., Saglia, R. P., & Gerhard, O. E. 1994, *MNRAS*, 269, 785+
- Bettoni, D. 1992, *A&AS*, 96, 333
- Binney, J., & Tremaine, S. 1987, *Galactic dynamics* (Princeton, NJ, Princeton University Press, 1987, 747 p.)
- Binney, J. J., Davies, R. L., & Illingworth, G. D. 1990, *ApJ*, 361, 78
- Bonfanti, P., Rampazzo, R., Combes, F., Prugniel, P., & Sulentic, J. W. 1995, *A&A*, 297, 28
- Bregman, J. N., Miller, E. D., Athey, A. E., & Irwin, J. A. 2005, *ApJ*, 635, 1031
- Bregman, J. N., Otte, B., Miller, E. D., & Irwin, J. A. 2006, preprint (astro-ph/0602524)
- Brighenti, F., & Mathews, W. G. 1996, *ApJ*, 470, 747+
- 1997, *ApJ*, 490, 592+
- 1998, *ApJ*, 495, 239+
- 2000, *ApJ*, 539, 675
- 2006, preprint (astro-ph/0601555)
- Buote, D. A., & Canizares, C. R. 1994, *ApJ*, 427, 86
- 1996, *ApJ*, 468, 184+
- 1997, *ApJ*, 474, 650+
- Buote, D. A., Jeltema, T. E., Canizares, C. R., & Garmire, G. P. 2002, *ApJ*, 577, 183
- Buote, D. A., Lewis, A. D., Brighenti, F., & Mathews, W. G. 2003, *ApJ*, 594, 741
- Cappellari, M., Bacon, R., Bureau, M., Damen, M. C., Davies, R. L., de Zeeuw, P. T., Emsellem, E., Falc3n-Barroso, J., Krajn3vić, D., Kuntschner, H., McDermid, R. M., Peletier, R. F., Sarzi, M., van den Bosch, R. C. E., & van de Ven, G. 2006, *MNRAS*, 366, 1126
- Cappellari, M., & Copin, Y. 2003, *MNRAS*, 342, 345
- Carollo, C. M., & Danziger, I. J. 1994a, *MNRAS*, 270, 743+
- 1994b, *MNRAS*, 270, 523+
- Carollo, C. M., Danziger, I. J., & Buson, L. 1993, *MNRAS*, 265, 553+
- Ciotti, L., & Pellegrini, S. 2004, *MNRAS*, 350, 609
- Cox, T. J., Dutta, S. N., Di Matteo, T., Hernquist, L., Hopkins, P. F., Robertson, B., & Springel, V. 2006, *ArXiv Astrophysics e-prints*
- Davies, R. L., & Birkinshaw, M. 1988, *ApJS*, 68, 409
- Dekel, A., Stoehr, F., Mamon, G. A., Cox, T. J., Novak, G. S., & Primack, J. R. 2005, *Nature*, 437, 707
- Diehl, S., & Statler, T. S. 2005, *ApJ*, 633, L21
- 2006, *MNRAS*, 368, 497
- 2007a, *ApJ*, to be submitted
- 2007b, *ApJ*, to be submitted
- D’Onofrio, M., Zaggia, S. R., Longo, G., Caon, N., & Capaccioli, M. 1995, *A&A*, 296, 319+
- Ellis, S. C., & O’Sullivan, E. 2006, *MNRAS*, 367, 627
- Fabbiano, G., Kim, D.-W., & Trinchieri, G. 1994, *ApJ*, 429, 94
- Falc3n-Barroso, J., et al. 2006, in preparation
- Finoguenov, A., & Jones, C. 2001, *ApJ*, 547, L107
- Fisher, D. 1997, *AJ*, 113, 950+
- Flores, R. A., Allgood, B., Kravtsov, A. V., Primack, J. R., Buote, D. A., & Bullock, J. S. 2005, *ArXiv Astrophysics e-prints*
- Forman, W., Jones, C., & Tucker, W. 1985, *ApJ*, 293, 102
- Fukazawa, Y., Botoya-Nones, J. G., Pu, J., Ohto, A., & Kawano, N. 2006, *ApJ*, 636, 698
- Garcia, A. M. 1993, *A&AS*, 100, 47
- Gerhard, O., Kronawitter, A., Saglia, R. P., & Bender, R. 2001, *AJ*, 121, 1936
- Goudfrooij, P., Hansen, L., Jorgensen, H. E., Norgaard-Nielsen, H. U., de Jong, T., & van den Hoek, L. B. 1994, *A&AS*, 104, 179
- Graham, A. W., Colless, M. M., Busarello, G., Zaggia, S., & Longo, G. 1998, *A&AS*, 133, 325
- Hanlan, P. C., & Bregman, J. N. 2000, *ApJ*, 530, 213
- Humphrey, P. J., & Buote, D. A. 2006, *ApJ*, 639, 136

- Humphrey, P. J., Buote, D. A., Gastaldello, F., Zappacosta, L., Bullock, J. S., Brighenti, F., & Mathews, W. G. 2006, *ApJ*, 646, 899
- Irwin, J. A., Athey, A. E., & Bregman, J. N. 2003, *ApJ*, 587, 356
- Jarrett, T. H., Chester, T., Cutri, R., Schneider, S., Skrutskie, M., & Huchra, J. P. 2000, *AJ*, 119, 2498
- Jarrett, T. H., Chester, T., Cutri, R., Schneider, S. E., & Huchra, J. P. 2003, *AJ*, 125, 525
- Jones, C., Forman, W., Vikhlinin, A., Markevitch, M., David, L., Warmflash, A., Murray, S., & Nulsen, P. E. J. 2002, *ApJ*, 567, L115
- Keeton, C. R. 2001, *ApJ*, 561, 46
- Khosroshahi, H. G., Jones, L. R., & Ponman, T. J. 2004, *MNRAS*, 349, 1240
- Killeen, N. E. B., & Bicknell, G. V. 1988, *ApJ*, 325, 165
- Kley, W., & Mathews, W. G. 1995, *ApJ*, 438, 100
- Lintott, C. J., Ferreras, I., & Lahav, O. 2006, *ApJ*, 648, 826
- Loewenstein, M., & White, III, R. E. 1999, *ApJ*, 518, 50
- Longhetti, M., Rampazzo, R., Bressan, A., & Chiosi, C. 1998, *A&AS*, 130, 267
- Longo, G., Zaggia, S. R., Busarello, G., & Richter, G. 1994, *A&AS*, 105, 433
- Machacek, M., Dosaj, A., Forman, W., Jones, C., Markevitch, M., Vikhlinin, A., Warmflash, A., & Kraft, R. 2004, preprint (astro-ph/0408159)
- Mamon, G. A., & Lokas, E. L. 2005, *MNRAS*, 362, 95
- Mathews, W. G., & Brighenti, F. 2003a, *ARA&A*, 41, 191
- 2003b, *ApJ*, 599, 992
- Meza, A., Navarro, J. F., Steinmetz, M., & Eke, V. R. 2003, *ApJ*, 590, 619
- Nagai, D., Vikhlinin, A., & Kravtsov, A. V. 2007, *ApJ*, 655, 98
- Napolitano, N. R., Romanowsky, A. J., Douglas, N. G., Capaccioli, M., Arnaboldi, M., Kuijken, K., Merrifield, M. R., Freeman, K. C., & Gerhard, O. 2004, *Memorie della Societa Astronomica Italiana Supplement*, 5, 255+
- Osmond, J. P. F., & Ponman, T. J. 2004, *MNRAS*, 350, 1511
- O'Sullivan, E., Forbes, D. A., & Ponman, T. J. 2001, *MNRAS*, 328, 461
- O'Sullivan, E., & Ponman, T. J. 2004, *MNRAS*, 354, 935
- Padmanabhan, N., Seljak, U., Strauss, M. A., Blanton, M. R., Kauffmann, G., Schlegel, D. J., Tremonti, C., Bahcall, N. A., Bernardi, M., Brinkmann, J., Fukugita, M., & Ivezić, Ž. 2004, *New Astronomy*, 9, 329
- Palimaka, J. J., Bridle, A. H., Brandie, G. W., & Fomalont, E. B. 1979, *ApJ*, 231, L7
- Paolillo, M., Fabbiano, G., Peres, G., & Kim, D.-W. 2003, *ApJ*, 586, 850
- Paturel, G., Andernach, H., Bottinelli, L., di Nella, H., Durand, N., Garnier, R., Gouguenheim, L., Lanoix, P., Marthinet, M. C., Petit, C., Rousseau, J., Theureau, G., & Vauglin, I. 1997, *A&AS*, 124, 109
- Peletier, R. F., Davies, R. L., Illingworth, G. D., Davis, L. E., & Cawson, M. 1990, *AJ*, 100, 1091
- Pellegrini, S., & Ciotti, L. 2006, *ArXiv Astrophysics e-prints*
- Pellegrini, S., Held, E. V., & Ciotti, L. 1997, *MNRAS*, 288, 1
- Prugniel, P., & Simien, F. 1994, *A&A*, 282, L1
- Prugniel, P., Zasov, A., Busarello, G., & Simien, F. 1998, *A&AS*, 127, 117
- Rasia, E., Ettori, S., Moscardini, L., Mazzotta, P., Borgani, S., Dolag, K., Tormen, G., Cheng, L. M., & Diaferio, A. 2006, *MNRAS*, 369, 2013
- Rasia, E., Tormen, G., & Moscardini, L. 2004, *MNRAS*, 351, 237
- Romanowsky, A. J., Douglas, N. G., Arnaboldi, M., Kuijken, K., Merrifield, M. R., Napolitano, N. R., Capaccioli, M., & Freeman, K. C. 2003, *Science*, 301, 1696
- Romanowsky, A. J., & Kochanek, C. S. 1998, *ApJ*, 493, 641+
- Ryden, B. S. 1996, *ApJ*, 461, 146
- Sarazin, C. L., Kundu, A., Irwin, J. A., Sivakoff, G. R., Blanton, E. L., & Randall, S. W. 2003, *ApJ*, 595, 743
- Schindler, S. 1996, *A&A*, 305, 756
- Shadmehri, M., & Ghanbari, J. 2002, *ApJ*, 574, 198
- Simien, F., & Prugniel, P. 1997a, *A&AS*, 122, 521
- 1997b, *A&AS*, 126, 15
- 1998, *A&AS*, 131, 287
- 2002, *A&A*, 384, 371
- Sofue, Y., & Rubin, V. 2001, *ARA&A*, 39, 137
- Springel, V., White, S. D. M., Jenkins, A., Frenk, C. S., Yoshida, N., Gao, L., Navarro, J., Thacker, R., Croton, D., Helly, J., Peacock, J. A., Cole, S., Thomas, P., Couchman, H., Evrard, A., Colberg, J., & Pearce, F. 2005, *Nature*, 435, 629
- Statler, T. S., Dejonghe, H., & Smecker-Hane, T. 1999, *AJ*, 117, 126
- Statler, T. S., & McNamara, B. R. 2002, *ApJ*, 581, 1032
- Sugerman, B., Summers, F. J., & Kamionkowski, M. 2000, *MNRAS*, 311, 762
- Tonry, J. L., Dressler, A., Blakeslee, J. P., Ajhar, E. A., Fletcher, A. B., Luppino, G. A., Metzger, M. R., & Moore, C. B. 2001, *ApJ*, 546, 681
- Tremblay, B., & Merritt, D. 1995, *AJ*, 110, 1039
- Vincent, R. A., & Ryden, B. S. 2005, *ApJ*, 623, 137
- Voit, G. M., Bryan, G. L., Balogh, M. L., & Bower, R. G. 2002, *ApJ*, 576, 601
- Xu, H., Kahn, S. M., Peterson, J. R., Behar, E., Paerels, F. B. S., Mushotzky, R. F., Jernigan, J. G., Brinkman, A. C., & Makishima, K. 2002, *ApJ*, 579, 600